Organic dendritic fibers: novel interfaces for bioelectronics and biohybrid computing

Politecnico di Torino

1859

Supervisors:
Prof. Carlo Ricciardi
Prof. Luisa Petti
Dr. Giuseppe Ciccone

Candidate:
Matteo Boggiatto

Thought to stand alone
Found the need of many

A Martina

Abstract

The human brain exhibits remarkable computational capabilities, inspiring research in both neuromorphic computing and bioelectronic neural interfaces, trying to harness its full potential. Organic mixed ionic-electronic conductors (OMIECs) such as poly(3,4-ethylenedioxythiophene) (PEDOT) have been extensively studied for their role in extracellular neural recording and stimulation, benefiting from their high biocompatibility, porosity, and electrical properties. In parallel, dendritic PEDOT fibers have emerged as promising candidates for neuromorphic computing due to their ability to replicate key synaptic functionalities and to be scaled into networks capable of performing complex computations within reservoir computing systems. Furthermore, optically responsive organic semiconductors such as poly(3-hexylthiophene) (P3HT) have gained interest for neural interfacing, enabling optical stimulation without genetic modifications.

Despite advances in these fields, bioelectronic neural interfaces and neuromorphic computing have only been explored independently. The integration of these two domains into a unified platform remains an open challenge. Beyond this, the development of dendritic fibers that combine both neuromorphic and optoelectronic functionalities represents a promising direction for further advancing both domains.

Here, a preliminary step toward the convergence of these fields is proposed, with the fabrication of a unified platform based on dendritic OMIEC fibers. Specifically, PEDOT-based fibers were intended to support synaptic-like behavior within the structure, while P3HT was integrated to introduce optical responsiveness. The fabrication process was optimized to ensure compatibility with neural cell cultures, establishing conditions for stable growth and interaction with the polymeric structures.

Experimental results confirm the feasibility of generating photovoltage within the dendritic fibers with measured peaks of $50\,mV$, compatible with the standarst of cellular stimulation. This highlights their potential for optically driven neuromorphic processes. Additionally, cell viability assessments indicate that the proposed system supports neural cell adhesion and proliferation, reinforcing its suitability for biohybrid applications.

These findings pave the way for an organic, biocompatible platform, with the possibility of further functionalization, bridging biological and artificial neural networks. By integrating neuromorphic processing with optically addressable bioelectronic interfaces, this work opens new perspectives for advanced brain-inspired computing and neural interfacing.

Contents

CHAPTER 1

Introduction: theory and applications

1.1 Motivation

The human brain is an extraordinarily complex system with outstanding computational capabilities, making it a subject of study in fields ranging from medicine to artificial intelligence, with the aim of understanding and harnessing its full potential. To this end, two possibilities are generally explored: direct *in-vivo* or *in-vitro* study through devices and interfaces in contact with neurons, or mimicking its functions, as investigated in the field of neuromorphic computing.

The first approach encompasses numerous studies focused on enhancing the performance of devices and electrodes for extracellular recording and stimulation. To do so, research has investigated various electrode geometries and materials. Among these, poly(3,4-ethylenedioxythiophene) (PEDOT), a conductive organic polymer, has gained particular attention due to its intrinsic porosity, which leads to improved cell adhesion, lower impedance, and consequently enhancing the signal-to-noise ratio[1,2].

Moreover, in this field, there is a growing interest in solutions that allow cellular optical stimulation without requiring genetic modifications. One promising approach involves using organic polymers capable of generating a voltage in solution upon exposure, poly(3-hexylthiophene) (P3HT)[3,4].

Further interest in these materials arises from their inherent biocompatibility and highly porous polymeric structure, closely mimicking the natural extracellular matrix. This similarity can significantly enhance cell viability and promote effective proliferation on the substrate.

On the other hand, PEDOT has been investigated within neuromorphic computing to emulate the exceptional functionalities of the brain. Specifically, dendritic PEDOT fibers have been extensively studied, showing their ability to replicate a good number of neuronal synaptic functions[5,6,7]. Moreover, when multiple fibers are integrated into networks, their complex mutual interactions can be exploited for reservoir computing[8]. Systems based on such networks have demonstrated the ability to perform complex computational tasks, such as classification of biological signals.

Until now, biocompatible neural interfaces and neuromorphic computing have been explored separately. The critical next step, therefore, is to integrate these two approaches into a unified platform, leveraging their possibilities. The dendritic morphology of the aforementioned fibers can further enhance the bio-mimetic potential of organic polymers, as they resemble natural neuronal structures. Additionally, the presence of cells within a fiber network could lead to unexplored reciprocal interaction dynamics.

A further step forward is to go beyond PEDOT fibers by developing photostimulable dendritic fibers. This can be achieved by integrating P3HT in their fabrication process, expanding the possibilities to new complex dynamics from optical stimuli.

This research lays the groundwork for an organic, biocompatible platform with the possibility of further functionalization, bridging biological neural networks with artificial neuromorphic systems. The key step toward this goal is demonstrating the feasibility

of fabricating dendritic fibers compatible with the aforementioned systems and, for the first time, integrating two polymers into their fabrication to achieve photovoltage generation. This experimental work was conducted at the Free University of Bolzano, within the Sensing Technologies Lab, whereas the tests on biological samples were conducted in Eurac Research laboratories by Giovanna Gentile. These studies were developed from their foundations, starting with the experimental design of the device and fabrication process, followed by the establishment of protocols for obtaining the fibers and assessing cell viability on them.

In the following sections, a more extensive overview will be provided. First, the theoretical framework of the topics addressed in this thesis will be introduced, followed by a discussion on how the relevant properties can be exploited to achieve the objectives of this work. Sec. 1.2 presents the main properties and characteristics of the materials investigated in this study, namely organic mixed ionic-electronic conductors (OMIECs), with a particular focus on their conduction mechanisms and doping processes. Subsequently, the basic principles governing the interaction between electrolytes and conductors will be reviewed in Sec. 1.3. The techniques employed to obtain the polymers will then be described, both in dendritic form (Sec. 1.4.1) and as thin films (Sec. 1.4.2). Finally, the applications of these techniques will be presented in detail. This begins with an in-depth analysis of how conductance modulation is achieved in dendritic fibers, starting from the operating principles of the devices that exploit OMIEC properties—namely, organic electrochemical transistors (OECTs) (Sec. 1.5.1). From there, the focus will shift to the evolution of these systems toward dendritic morphologies and their demonstrated potential for neuromorphic computing applications (Sec. 1.5.2). Next, the use of OMIECs to study brain functionality through cell-interface platforms will be discussed (Sec. 1.5.3). Lastly, the final section will highlight the emerging opportunities offered by P3HT in advancing beyond previous applications. In particular, its interaction with electrolytes combines electrochemical and optical properties, enabling the development of photoelectrochemical cells (PEC)(Sec. 1.5.4).

1.2   Organic mixed ionic-electronic conductors (OMIECs)

Conventional electronic materials often face significant challenges when used in biological environments, where factors such as biocompatibility and exposure to wet conditions can hinder performance. In light of these limitations, there has been growing interest in exploring new classes of materials that can better meet the demands of bioelectronics. Recently, organic materials have gained attention for their potential to address these issues and enable more effective integration with biological systems[9]. These materials, known as organic mixed ionic-electronic conductors (OMIECs), are polymers or polymer blends capable of conducting both electrons, due to their π-conjugated backbone, and ions from the surrounding electrolyte, thanks to their porosity and ion affinity. A particularly intriguing property of these materials is the strong dependence of their electronic resistance on the ion content within the polymeric matrix. This characteristic becomes especially valuable when the ion concentration can also be actively controlled. A first general description of OMIECs' behavior can be introduced in terms of their response to an applied voltage. Taking into account both the polymeric backbone and the electrolytic solution, when a voltage V is applied across the material, the total current density J will have four main contributors: holes, electrons, anions, and cations.

Regarding the electronic component, most OMIECs are based on conjugated polymers whose conduction relies on the formation of polarons along their π-backbone, making them predominantly hole-transporting materials. The specifics of this transport mechanism will be discussed in Sec. 1.2.1; for now, it is sufficient to note that for these materials hole mobility is typically much higher than electron mobility. For instance, poly(3,4-ethylenedioxythiophene) polystyrene sulfonate (PEDOT:PSS) exhibits a hole mobility of $\mu_h = 0.1\, cm^2 s^{-1} V^{-1}$, a value three orders of magnitude higher than the one measured for electrons[10,11].

On the other hand, due to their greater mass, ions in the electrolyte generally exhibit significantly lower mobility compared to holes. For example, sodium ions in an aqueous sodium chloride (NaCl) solution have a mobility of $\mu_h = 10^{-4}\, cm^2 s^{-1} V^{-1}$, a value that has been shown to hold even within the polymeric matrix, owing to the material's large porosity[12].

Thus the current can be simplified as

$$I = e\rho_h \mu_h \frac{Wt}{L} V$$

with te corresponding resistance being:

$$R = \frac{V}{I} = \left(\rho_h \mu_h \frac{Wt}{L} \right)^{-1}$$

Where V and I are the voltage across the material ann the current flowing through it. W, t and L are the geometrical dimensions of the material, namely the width, the thickness, and the length, e is the unitary charge, ρ_h charge density of holes, μ_h is the hole mobility.

Another key parameter is then is the charge concentration ρ_h, which is directly related to the doping level of the material; Compared to their inorganic counterparts, OMIECs require a much higher doping level, typically exceeding $\rho = 10^{20}\,cm^{-3}$. More details about the conduction mechanism, the involved carriers, and the doping mechanism will be given in Sec. 1.2.1 and 1.2.3

1.2.1   Electronic transport in OMIECs

As mentioned above, the electronic conduction in OMIECs is enabled by the typical molecular structure present in conjugated polymers, the $pi-$backbone. Indeed, in these materials the overlap of π-orbitals in their double bonds, generate a delocalization of electronic states along the whole polymer chain, enabling conduction

In any conjugated polymer, the two most important energy levels are the highest occupied molecular orbital (HOMO) and the lowest unoccupied molecular orbital (LUMO), whose separation, known as the HOMO-LUMO gap (HLG), plays a crucial role in various in their conductive and optical properties. In organic polymers energy bands (valence and conduction) are not well defined as for crystalline inorganic materials. Indeed, the bonding states are scattered into a valence-band-like set of HOMO states, while antibonding states give rise to a conduction-band-like set of LUMO states, with a density of states that can be approximated by a Gaussian distribution (Fig.1.1b).

In their neutral state, the valence band is filled while the conduction band remains empty, making the polymer an intrinsic semiconductor with a low charge carrier concentration and a large bandgap. When an electron is removed, the polymer undergoes oxidation, breaking one of the double bonds in the π-backbone and creating a vacancy, namely a hole. This charge introduction induces a structural distortion in the chain, which moves along with the free charge, forming a quasiparticle known as a polaron. The polarons states are organized in their own band, with a distribution in energy similar to the one described for the HOMO and LUMO states. In Fig.1.1, the electronic structure corresponding to this descriprion conditions of high disordered polymers towards more ordered one is displayed.

Whether the doping level is very high, the conductivity of the polymer chain is still limited by the mobility, with the irregular arrangement of molecules due to thermal vibrations being one of the main limiting factors. Thus, the electronic transport in OMIECs can be modeled as a temperature-activated hopping mechanism, where charge carriers move through sequential jumps between sites, corresponding to local minima in the energy landscape. The most comprehensive picture of transport in these polymers has been laid out by Bubnova *et al.*[10], where the hopping transport is combined with a study of the band structure of the polymer.

Within the disordered bulk of conjugated polymers, more ordered domains can emerge due to weak intermolecular interactions, such as $\pi - \pi$-stacking between adjacent chains. These interactions can give rise to semi-crystalline or lamellar structures, where segments of different chains align and interact, contributing to the overall charge transport properties. Different types of hopping mechanisms can be distinguished: a faster one,
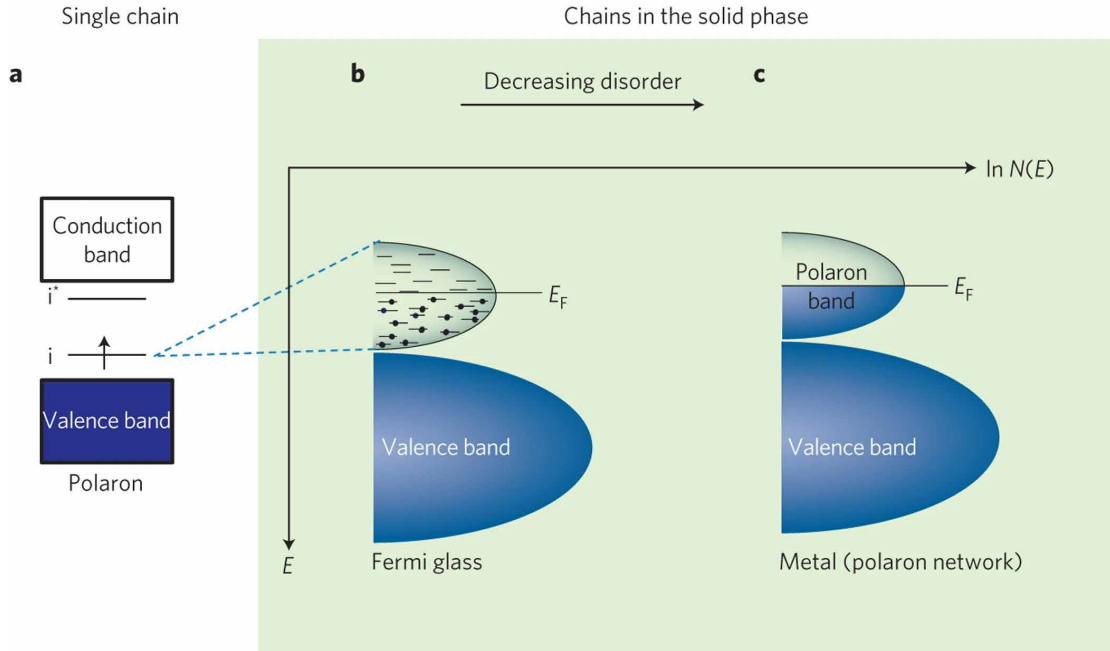
Figure 1.1: Electronic band structure of conjugated polymers corresponding description in conditions of high disordered polymers and higher ordered ones. Electronic structure of a polymer chain with one polaron (a), sketch of the logarithm of the density of states (DOS, lnN(E)) for an amorphous polaronic polymer solid with localized states around the Fermi level (E_F) (b), as well as for a metallic network of polarons with the Fermi level lying in a delocalized polaron band (c). In the electronic structures, i and i* represent the in-gap states induced by local structural distortions. Image taken from Bubnova *et al.*[10].

associated to hopping along the scattered states of the polymeric chain (intra-chain), and a slower one, characterized by inter-chain jumps from one backbone to another. The different organization of the polymer chains can thus affect the conduction within this latter mechanism. Such polymers could be more or less organized, even in semicrystalline or lamellar structures[13,14,15].

1.2.2   Ionic transport in OMIECs

Due to the relatively high resistance of electrolytic solutions, their impact on OMIEC conductivity is often minimal. However, in specific cases, the electronic conduction is deliberately suppressed, the ionic contribution can become significant.
The mechanisms governing ionic transport in polymers remain largely unexplored and are commonly approximated using diffusion models. In this context, the diffusion coefficient D is related to ionic mobility through the Einstein relation:

$$D = \mu_i k_b T$$

While a comprehensive discussion on ionic dynamics is beyond the scope of this thesis, it is important to note that ion transport predominantly occurs through the liquid phase within the polymer matrix. For this process to be efficient, the polymer must absorb

enough solvent to support ion motion. Moreover, it has been confirmed that for polymers like PEDOT, the mobility of ions remains unchanged within the bulk solution and polymer matrix[12]

1.2.3 Doping in conjugated polymers

In inorganic semiconductors, doping is achieved by introducing atomic impurities to modulate carrier concentration. As described in Sec. 1.2, in conjugated polymers, the generation of free carriers is mediated by redox processes, involving the oxidation of a double bonding. For this reason, the doping of these matrial must rely on alternative mechanisms that fit in such a "chemical" frame, such as molecular or electrochemical doping.

Electrochemical doping in conductive polymers

In organic semiconductors, the presence of high impurity levels requires an equally high doping concentration to effectively modulate their electrical properties. As presented in Sec. 1.2.1, unlike their inorganic counterparts, these materials do not exhibit well-defined energy bands but rather a series of discrete states, thus necessitating a different approach to doping.

Doping in organic semiconductors is better described in chemical terms: the removal of an electron from a neutral molecule M generates a radical cation M^+, a process known as oxidation. This mechanism is particularly favored in π-conjugated systems, where resonance stabilization facilitates charge delocalization. When subjected to an appropriate electrostatic environment, a fraction of the polymer monomeric units oxidizes, undergoing bond rearrangement and leading to emergence of free charge carriers. This structural and electronic modification gives rise to a polaron, a quasi-particle composed of the charge itself and the associated lattice distortion.

Due to the nature of these electronic states in conjugated polymers, hole generation is generally more favorable through oxidation processes, making them predominantly hole-transporting materials. Among OMIECs, one of the most extensively studied examples is PEDOT:PSS, whose doping mechanism will be further explored in the following sections.

PEDOT:PSS

PEDOT:PSS is a widely used conductive polymer blend, consisting of PEDOT, which provides a π-conjugated backbone enabling hole transport, and PSS, which acts as a dopant. Studies have shown that these two components do not mix uniformly but rather form distinct PEDOT-rich and PSS-rich domains (Fig. 1.2a). The doping process primarily occurs at the interface between these domains, where charge transfer between PEDOT and PSS influences the material's electronic properties.
This results in a charge carrier concentration that can reach approximately $10^{20} cm^{-3}$, effectively reducing the intrinsic bandgap of PEDOT and enabling efficient charge injection from various metals, particularly gold.

PEDOT exhibits significant hygroscopicity, leading to moisture absorption and poten-
tial degradation in dry electronic applications. However, this property, combined with
the hydrophilicity of PEDOT:PSS, has been exploited in emerging electronic systems
designed for operation in wet environments. When exposed to water, PEDOT:PSS func-
tions as an effective OMIEC, undergoing two key processes: swelling and dedoping.
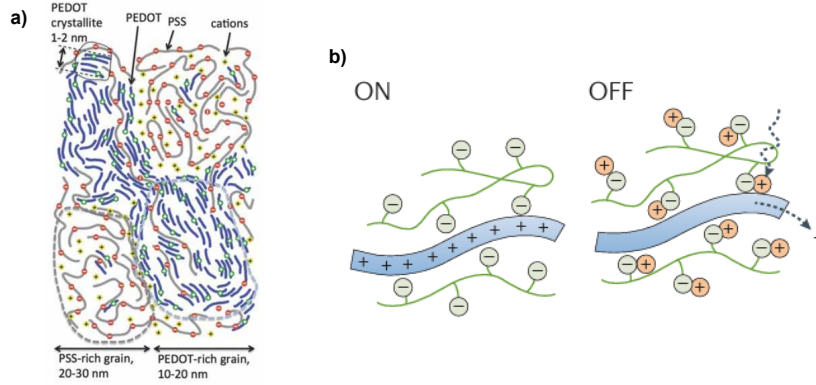
Figure 1.2: Sketches of some properies of PEDOT:PSS. (a) inhomogeneous morphology of PE-
DOT:PSS from Volkov *et al.* [16]. (b) dedoping mechanism: when the cations in the solution
interfere with the doping anions, the charge density in the polymer is reduced and the conduc-
tion is switched off. Image adapted from [17]

Swelling occurs as water molecules and ions infiltrate the polymer matrix, causing an
expansion of up to 60% of its original volume. Once fully hydrated, dissolved ions
can interact with the material, altering its electronic properties as swown in Fig. 1.2b.
In particular, cations from the electrolyte can associate with the SO_3^- groups of PSS,
following the redox reaction:

$$PEDOT^+ + PSS^- + Na^+ + Cl^- + e^- \rightarrow PEDOT^0 + Na^+ + PSS^- + Cl^-$$
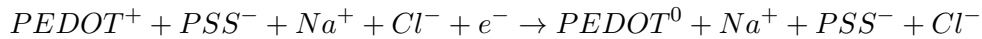
This dedoping process plays a fundamental role in the functionality of OMIEC-based
devices. In this work, rather than focusing on the microscopic organization of PEDOT,
dopant, and ions, we will assume a homogeneous distribution, as a detailed morphological
study is beyond the scope of this thesis.

PEDOT:PSS is the most recurrent material in organic electronics, but many more sys-
tems, such as PEDOT:PF6 and P3HT:PF6 follow the same fundamental principles de-
scrived above. As detailed in the abstract, in this thesis we will focus mostly on these
alternative systems.

1.3   Electrolytes interfaces

An electrolyte is a medium that contains freely moving cations and anions, allowing ionic conduction. Focusing on liquid electrolytes, the transport of charge in these solutions is primarily governed by the motion of ions, which, due to their larger mass compared to electrons, exhibit higher scattering and lower mobility.

It is important to note that both anions and cations contribute to ionic conduction. Only in cases where one species moves significantly faster than the other, it is possible to approximate the system as single-species transport. The effective size of an ion is largely influenced by its solvation shell, which consists of solvent molecules surrounding the ion. The characteristic dimension of this shell depends on the charge density of the ion: smaller, highly charged ions create stronger local electric fields, leading to larger solvation shells and, consequently, higher resistance.

Additionally, the dynamics of dissolved salts play a crucial role in polymerization and influence ionic concentration. For simplicity, in this discussion, we will assume ideal conditions, neglecting ion-ion interactions and considering electrolyte concentrations in the millimolar (mM) range.

Metal/electrolyte interfaces and electrical double layer

When a voltage is applied to an electrode in an electrolytic solution, two possible phenomena can occur at the interface: the electrode may undergo a redox reaction with the ions in the solution, or it may act as an inert surface where ions accumulate

A classic example of an electrode reaction is that of a silver/silver chloride (Ag/AgCl) electrode, which undergoes the following redox process in the presence of dissolved Na^+ ions:

$$AgCl + Na^+ + e^- \rightarrow Ag^0 + NaCl$$

In this case, each sodium ion reaching the electrode surface facilitates the transfer of an electron, sustaining the reaction and generating a measurable current. This results in the depletion of excess ions near the interface, where the corresponding voltage drop can be described by the Nernst equation:

$$\Delta V_{GE} = \frac{k_B T}{q} \ln \left(\frac{[c_{e,\text{outside}}]}{[c_{e,\text{inside}}]} \right)$$

where $[c_e]$ is the electrolyte concentration. Ag/AgCl electrodes in saline solutions are classified as non-polarizable and can be approximated as resistive elements.

Conversely, when an electrode does not participate in chemical reactions with either the solvent or the ions, the charge carriers accumulate at the interface, forming what is known as the electrical double layer (EDL). This layer consists of a dense region of counterions adsorbed onto the electrode surface, followed by a more diffuse region extending into the electrolyte. The EDL plays a crucial role in electrochemical systems, as it de-

termines charge screening, capacitance, and interfacial potential behavior. Electrodes that primarily exhibit this behavior are termed polarizable and are typically modeled as capacitive elements. In practice, real metal/electrolyte interfaces exhibit both resistive and capacitive characteristics, requiring a more complex equivalent circuit representation. In general material/electrolyte interface is modeled as a Randles cell, represented in Fig. 1.3, where R_{CT} is the resistance associated to the non polarizable contact, C_{DL} is the capacitance related to the electrical double layer and R_S is the resistance of the solution.
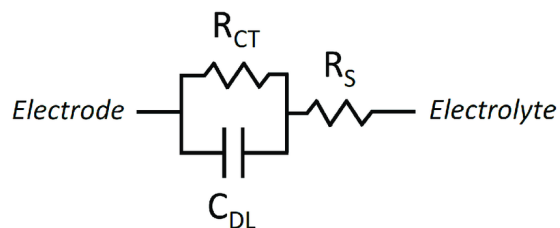
Figure 1.3: Schematic representation of the simplified Randles circuit commonly used to model electrode/electrolyte interfaces.

1.4 Electro-polymerization techniques

1.4.1 Field directed polymerization (FDP)

Field-directed polymerization (FDP) is a technique that enables the fabrication of polymer fibers whose topology can be modulated by adjusting the parameters of an applied AC signal. In the work of Cucchi *et al.*[6], FDP is presented as a cost-effective and alternative method for the fabrication of OECT channels, which will be discussed in Sec. 1.5.1. Many works explored different growth setups and conditions, exploring the possibility of tuning the morphological and electrical characteristics of the fibers to emulate a good number of synaptic properties[18,19,20,21,22,23,24]. In particular, the relationship between polymer growth and the applied signal was investigated and modeled in the study of Ciccone *et al.*[25]. The considerations reported in these studies provide the foundational basis for the reasoning developed in this work.

Moreover, in light of the current state of the art, fibers produced through FDP may offer a viable strategy for neuromorphic applications, leveraging an OMIEC such as PEDOT, which exhibits properties compatible with biological environments.

Growth mechanism of field directed polymerization

For the formation of organic dendritic networks, an electrolytic solution containing the precursor monomer must immerse the area between the two electrodes that will be bridged. The polymerization process requires the oxidation of a monomer, which occurs once the oxidation potential is reached, for example by applying a voltage. However, the monomer alone cannot polymerize; a counter ion is necessary to form a stable complex, enabling the polymerization reaction. In our case, for example, the monomer will be 3,4-ethylene-dioxythiophene (EDOT) and the counter ion is provided by tetrabutylammonium hexafluorophosphate (PEDOT:PF6), but this description can be extended to any monomer M and anion A^- that lead to a conductive polymer.

The polymerization process occurs in three main steps:

1. The application of a positive voltage exceeding the oxidation potential of monomer M leads to its radicalization at the electrode/electrolyte interface. Simultaneously, anions (A^-) drift toward the electrode, accumulating and forming an EDL. On the other hand the cations will drift towards the other electrode.

2. The radical cation M^+ is then neutralized by an A^- anion.

3. The neutralized complex M:A remains reactive and can interact with additional M^+ radicals, supplied both by the bulk solution and the growing polymer layer on the electrode.

Polymer growth occurs more rapidly in regions where the local electric field is stronger, as more A^- anions accumulate near the electrode. When a DC voltage is applied between two electrodes, the polymerization proceeds almost isotropically, as the ions accumulate more and more at the positive electrode surface, leading to a film-like coverage.

In contrast, applying an AC stimulus the ions can drift towards the electrode only for a limited amount of time. Indeed, the polymerization at an electrode is possible only during the positive semi-cycle, and as its duration decreases, the reaction will be confined to areas where the kinetics are faster, so that ions can reach these points form the polymer. Then fiber growth is favored in regions of higher local field where the drift is faster. As the process continues, the newly formed fibers further intensify the field at their extremities due to the "tip effect", reinforcing polymerization at the tips rather than at the base, following a mechanism analogous to a Faraday cage. In this way the polymerization tens to occur along a more linear path, proceeding from any new tip formed.

Any shape of waveform is possible, with the condition that it must contain both positive and negative polarities to sequentially attract and repel the ions. Restricting to square-waves, the available degrees of freedom to tune the polymerization are then the amplitude, the offset, the duty cycle and the frequency of the signal. In the work of Ciccone *et al.*[25], it is shown how the strength and asymmetry of the signal influences the final result. The stronger the applied potential, the faster the accumulation of anions on the surface and, consequently, the faster the polymerization, leading to thicker fibers. This effect is directly linked to the strength of the electric field, which increases as the gap between the electrodes decreases. Additionally, the field is further enhanced at electrode corners (if present), making the geometry of the contacts a crucial factor in determining the final outcome of the polymerization.

On the other hand, increasing the frequency reduces the time available for polymerization, leading to thinner fibers. The alternating signal can be described as "growth-ON" and "growth-OFF" phases for each electrode in the system. During the "growth-ON" phase, monomer is consumed, and new monomer diffuses to compensate for the generated concentration gradient. This diffusion is supposed to occur isotropically around the polymerization site, promoting the formation of branched fibers, splitting the polymerization direction in more than one site.
During the "growth-OFF" phase, the ions drift toward the opposite electrode, with a speed influenced by the mobility of the salt in solution. Faster ion drift results in more rapid redistribution, directly impacting the polymerization dynamics. In Fig. 1.4 a schematic of the fiber growth as reported in the work of Cucchi *et al.*[6].

During growth, multiple fibers branch out from the electrodes and extend along the field lines until they bridge the gap between the electrodes. Even after the first connection is established, polymerization continues at other sites, reinforcing the network and lowering resistance.
The growth process can be divided into three distinct stages. The first stage is characterized by fiber elongation without any bridged connections, resulting in high resistance. In the second stage, after the first connection and bridging of the electrodes, additional fibers emerge and add to the network, enhancing overall conductance (reinforcement). Finally, the process enters a saturation phase, where ionic transport in the solution becomes negligible, preventing further fiber growth[6]. This phase is rarely met in standard conditions, because usually the stopping condition is that when two fibers meet from opposite electrodes, as the newly formed "bridge" is so conductive that the majority
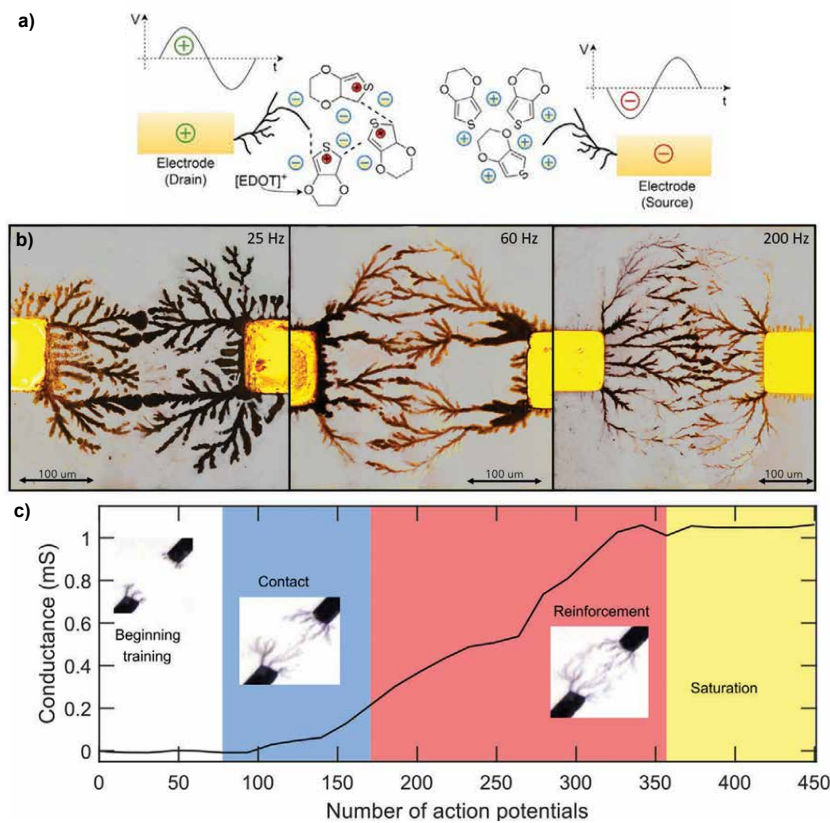
Figure 1.4: Set-up and growth of the dendritic PEDOT-based networks. a) Sketch of the polymerization process: during the positive polarity of the applied electrical signal, the anions oxidize the monomers at the interface and trigger the reaction; during the negative polarity, the monomer surrounded by cations is inert. b) Dependence of fiber morphology on the frequency of the applied signal: higher frequencies promote thinner fibers and a higher degree of bifurcation. c) Example of learning curve during the formation of the dendritic networks. Image adapted from [6].

of the current is passing through it, so that all the driving force is removed from the solution. An example of the evolution of the fiber conductance along the fiber growth is shown in Fig. 1.4d.

In conclusion, it is important to notice that the aforementioned polymerization parameters are then highly dependent on the geometry of the electrodes. Moreover, considerable losses must be accounted to evaluate the needed applied potential, since the electrode behaves as described in Sec. 1.3. Image from Cucchi *et al.*[6]

In conclusion, an almost trivial but fundamental detail is that this kind of polymerization is possible only if the polymer is conductive enough to extend the potential to its tips with negligible losses. Otherwise, it will just cover the contact, leading to contact passivation.

1.4.2   Cyclic voltammetry as polymerization technique

Cyclic voltammetry (CV) is an analytical technique used to study the thermodynamics and kinetics of electron transfer for a given analyte. It belongs to the class of voltammetric techniques as it involves a linear potential sweep. When the same sweep is reversed, it becomes cyclic, allowing the characterization of both oxidation and reduction processes occurring at the electrode.

The experimental setup consists of three electrodes: the working electrode (WE), where the potential is applied and the redox exchange takes place; the reference electrode (RE), whose potential is used as reference to impose the one at the WE; and the counter (or auxiliary) electrode (CE), which completes the circuit by allowing the flow of electrons to sustain the redox reaction. The operation is typically controlled by a potentiostat, which measures the current flowing between CE and WE, ploting it as a function of the applied potential. A typical voltammogram for a reversible redox reaction is shown in Fig. 1.5.

As the potential sweep proceeds and the conduction band of the WE aligns or surpasses the LUMO of the analyte at the surface, electron transfer occurs, resulting in analyte reduction. As the overlap between the electronic states increases, the current rises until it reaches a maximum, known as the cathodic peak. The same principle applies to oxidation, which involves the HOMO of the analyte, giving rise to the anodic peak. The existence of these peaks is related to the diffusion of new analyte molecules towards the WE, as diffusion becomes the limiting factor once the electron transfer process at the electrode occurs almost instantaneously. After reaching the peak, the current decreases and stabilizes at a constant value, known as the diffusion-limited current.
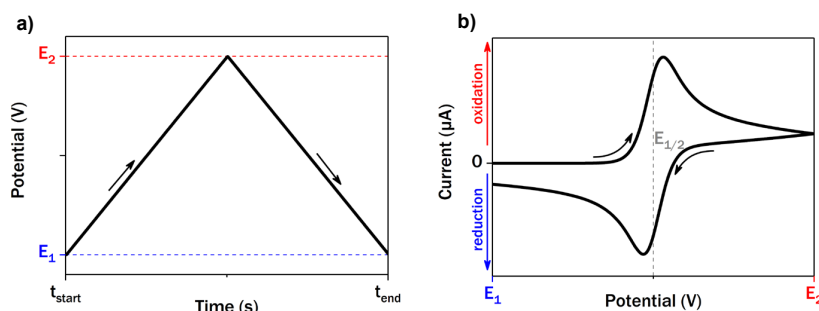
Figure 1.5: Example of voltage sweep and resulting voltammogram from a cyclic voltammetry. The voltage sweep is linear and its speed can be set with the scan rate, as the steepness of the curve. The sweep form E_1(negative) to E_2(positive), is the oxidative scan. The scan from E_2 to E_1 is the reductive scan. The resulting voltammogram features the measurements obtained in the two scans, with related oxidation and reduction peaks. $E_{1/2}$ corresponds to the median between the positions of the two peaks.

In this work, cyclic voltammetry was exploited as a polymerization technique. If the electrochemical window of the analyte is intentionally exceeded, electropolymerization can be triggered on the surface of the WE, with the same mechanism presented in Sec. 1.4.1, but with a voltage that varies linearly in time. The corresponding voltammogram ex-

hibits a sharp increase in current, followed by saturation and the appearance of a peak. During successive polarization cycles, the current generally increases progressively. This type of deposition is possible for redox-active materials, but successive scans can only be performed if the deposited material is conductive, as in the case of PEDOT:PF$_6$ and P3HT:PF$_6$. The idea of this kind of polymerization has been explored in many studies to obtain uniform PEDOT films[26,27,28,29] but also for thin P3HT films[30,31].

1.5   OMIECs applications

1.5.1   Organic Electrochemical Transistor

Within the field of electronics, one of the earliest and most significant applications explored is the transistor, particularly the Field-Effect Transistor (FET). When the channel is composed of an organic material, the device is referred to as an Organic Field-Effect Transistor (OFET). In such devices, a thin layer of organic semiconductor is separated from the metal gate electrode by a thin insulating layer (gate dielectric). When a voltage is applied between the gate and the channel, it induces a field-effect doping in the semiconductor, leading to the accumulation of mobile charge carriers at the interface with the dielectric. This charge in the channel is counterbalanced by a thin sheet of opposite charge on the gate electrode. The system behaves like a parallel-plate capacitor, and the accumulated charge can be estimated through the basic relation:

$$Q = C \cdot V$$

where C is the capacitance of the dielectric and V is the gate voltage generally calculated as

$$C = \epsilon_s \frac{A}{d}$$

where ϵ_s is the dielectric constant of the insulating material, A is the area of the plates and d is the dielectric thickness. In this configuration, the capacitance is inversely proportional to the dielectric thickness.

Starting from this working principle, a new type of transistor has been developed in the context of organic electronics, known as the Electrolyte-Gated Field-Effect Transistor (EG-FET). This device employs an alternative to the grate dielectric, namely an electrolyte interposed between the gate and the channel. When the channel is made of an organic material the device is called Electrolyte-Gated Organic Field-Effect Transistor (EGO-FET). When a voltage is applied on the gate, the ions are pushed towards the channel forming an EDL at the electrolyte–channel interface and at the gate-electrolyte interface. A sheet of ionic charge in the electrolyte compensates the induced sheet of electronic charge in the channel that enables the conduction. This configuration can be considered an extreme case of FET, because the thickness of the dielectric is reduced to dimensions on a par with the ionic radius, resulting in high capacitance.

The devices mentioned above, however, do not exploit the full potential of OMIECs as organic electrochemical transistors (OECTs). Such devices can be regarded as a specific class of EGO-FETs in which the channel consists of an OMIEC. Unlike traditional EGO-FETs, where ionic interactions are confined to the surface of the material, the ions in OECTs penetrate the porous polymer matrix, enabling volumetric charge modulation throughout the entire conductor. For this reason, it is more appropriate to refer to a volumetric capacitance C^*, rather than the conventional capacitance C mentioned above. The identifying characteristic of OECTs is that doping changes occur over the entire volume of the channel, as opposed to a thin interfacial region like in field-effect transistors (FETs). Therefore, large modulations in the drain current can be achieved

for low gate voltages, which makes OECTs efficient switches and powerful amplifiers. In Fig. 1.6 a schematic representation of the operating principles of the aforementioned devices.

If the polymer is already doped and thus conductive, as for example for PEDOT, the dedoping mechanism described in Sec. 1.2.3 can be exploited to suppress conduction. In the absence of a gate voltage, a hole current flows through the channel, meaning the device operates in the ON state. When a positive gate bias is applied, cations from the electrolyte are injected into the channel, compensate the fixed anions, and trigger dedoping. Therefore, the switching behavior of the material is directly influenced by the ease with which the salt ions can access the doping sites. Nonetheless, the initial doping level of the material determines the ON-state current. These considerations form the basis for the following discussion in the results section.
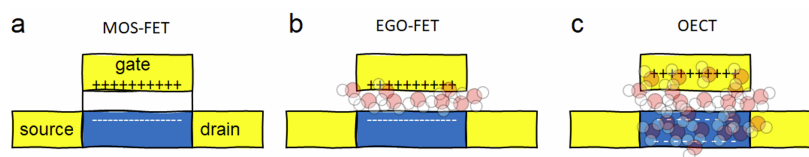
Figure 1.6: Difference between a traditional a) field effect transistor (FET), an b)electrolyte-gated organic FET (EGO-FET), and c) an organic electrochemical transistor (OECT). Although the architecture is similar, the operation mechanism differ substantially. In particular for EGO-FETs and OECTs, the solvent molecules interact with the channel and electrode materials and bring about new physical effects. The main difference between EGO-FETs and OECTs is that in the former, the solvent interact with the channel's interface, while in the latter, the solvent molecules can penetrate through the channel. Image adapted from [32].

For optimal device performance, it is essential that the gate capacitance significantly exceeds the channel capacitance, ensuring that most of the applied voltage drops across the channel/electrolyte interface. To achieve this, non-polarizable electrodes, whose capacitance can be approximated as infinite, are commonly employed as gate contacts. The gate electrode thus becomes a crucial component, and its material strongly affects the resulting characteristics.

Moreover, as described by Nernst equation, the gate/electrolyte voltage drop depends on the ion concentration. This dependency is directly reflected in the device's transfer characteristics, which makes OECTs naturally suited for applications as ion-sensitive sensors[33].

Although OECTs have been the subject of extensive research, a unified understanding of their operating mechanisms has yet to be reached. The scientific community remains divided on several aspects, and various models have been proposed to explain the device behavior under different conditions.

The first widely adopted model was introduced by Bernards *et al.*[34], which focused on describing the device operation in terms of key parametrs, like the carrier mobility and transconductance, namely the derivative of the drain current with respect to the gate voltage, with fixed drain voltage, that quantifies the sensitivity of the output current to changes in the input voltage. While this model proved effective in the linear regime,

it showed limitations when applied to the saturation region. Nonetheless, this model highlights once more the importance of transconductance in these devices, considering that the intrinsic porous nature of OECTs' channels leads to very high volumetric capacitances that can be exploited to increase the overall performances[35,36].

In the following years, several refinements were proposed to account for non-ideal behaviors[37,38]. More recently, thermodynamic approaches have been explored to develop a comprehensive framework capable of capturing the full range of OECT operation regimes[39].

1.5.2   Neuromorphic properties of polymer dendritic fibers

Starting from the development of OECTs, many studies investigated the possible applications in the field of neuromorphic computing. In particular in several studies Gkoupidenis *et al.*[5,40] demonstrated the possibility of emulate synaptic behaviors through a common gating of OECTs in the same electrolyte. Such global connectivity mediates the time-dependent interactions between all the devices that arise from the different time-constants of the ionic and electronic transport. Indeed, while the response of electronic carriers in the polymer backbone is almost instantaneous, ionic motion within the swollen polymer matrix occurs over a much slower timescale. As a result, the channel conductance remains modulated even after the electrical stimulus has ended, with retention times governed by ionic diffusion typically extending over hundreds of milliseconds. This delayed relaxation enables the emulation of *short-term plasticity* (STP), a key temporal feature of biological synapses[41].

From this point on, OECTs have been used to implement fundamental neuromorphic behaviors including potentiation, depression, and adaptation[42,43,44,45,46]. They can serve as basic building blocks for neuromorphic hardware, with the ability to either reconfigure the device morphology or interconnect multiple elements into functional networks.

In this framework, dendritic fiber based OECTs have been explored with exceptional results. The work by Janzakova[47] is particularly relevant in demonstrating *spike-timing dependent plasticity* (STDP). This was achieved by exploiting the temporal overlap between pre- and post-synaptic spikes to control the electropolymerization of dendritic connections. Through this mechanism, the effective growth of a conductive dendrite is driven by the overpotential generated during the overlap, with stronger and longer temporal correlations promoting irreversible growth, a structural counterpart of long-term potentiation.

The programmable nature of dendritic growth opens also the path to *structural plasticity*, where the connectivity pattern between nodes dynamically adapts to external stimuli[7,47]. This concept enables the transition from isolated synaptic elements to interconnected networks capable of collective response to input patterns. Such architectures have been investigated in the work of Cucchi *et al*[8], where the intrinsic randomness of dentrites find space for a reliable application in *reservoir computing* (RC). Here, the inherent non-volatility and temporal memory emerging from the different time constants between ionic and electronic, combined with the nonlinear behavior introduced by ionic-electronic coupling, are used to project input signals into a higher-dimensional space[48]. This transformation facilitates the separability of input features, making dendritic OECT networks a reliable platform for real-time signal classification. In Fig. 1.7 an example of reservoir node presented in the aforementioned work.

Beyond these implementations, recent studies have also highlighted the relevance of network topology as an active component of computation. In particular, the work of Scholaert *et al.*[49] emphasizes how the physical morphology and interconnectivity of PEDOT-based networks can influence the nonlinear dynamics of the system and enable in-memory processing. Although a detailed analysis of this approach lies beyond
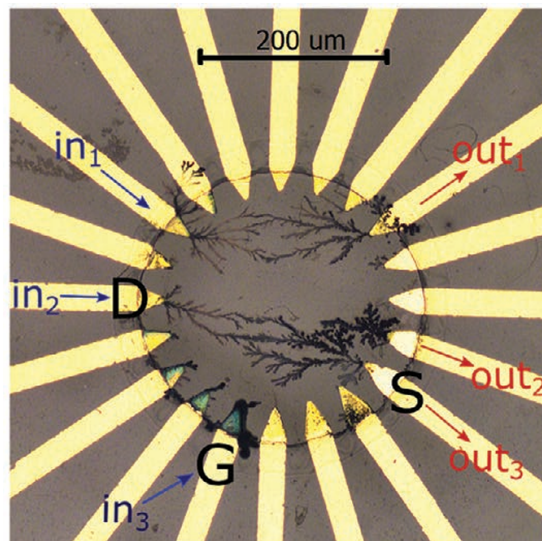
Figure 1.7: Photograph of a PEDOT:PF6 dendritic network used as a nonlinear node for reservoir computing. The leads on the left are the input of the reservoir and the leads on the right the output. Adapted from [8].

the scope of the present section, it represents a promising direction for the development of morphology-dependent computing architectures.

1.5.3 Cells' interfaces

As presented in the previous sections, the ability of OMIECs to operate in the same environment as living systems has opened new possibilities in bioelectronics. In this context, PEDOT stands out as a particularly suitable material. Its biocompatibility is broadly recognized within the scientific community, even with different dopants[50]. In fact PEDOT has already been investigated as a coating for metallic electrodes to enhance cell adhesion and improve the electrode–tissue interface[51,52,26,2]. Studies such as those by Nick *et al.*[27,53] have shown that PEDOT coatings reduce impedance and thermal noise while increasing the charge injection limit, thus enabling higher signal fidelity during neuronal recording and stimulation. These improvements are attributed to the enlarged electrochemical surface area and the mixed ionic-electronic conductivity of PEDOT, which facilitate more efficient coupling between the ionic currents of biological tissues and the electronic signals of the device. Building upon these advantages, recent studies have demonstrated the use of PEDOT-based OECTs as direct neural interfaces. As reported by Wu et al.[54], ultrathin, flexible OECTs fabricated from PEDOT:PSS enabled high-density, high signal-to-noise ratio (SNR) electrocorticography recordings on the cortical surface of rats, confirming their in vivo stability and functional performance.

On the other hand also P3HT has been proved to be biocompatible[55,56] and many studies focused on the uses of P3HT in biomedical applications, in particular trying to emulate the eye's retina[57,3,58]. Studies conducted by Vaquero *et al.*[4] explore the possibility of extracellular optical stimulation of cells, without need of genetic modification of the cells, exploiting the photogeneration mechanism presented in Sec.1.5.4.

These findings support the hypothesis that dendritic fibers may also serve as effective cell–device interfaces. Although, as previously discussed, the biocompatibility of PEDOT and P3HT as materials is well established, no studies to date have addressed how their morphology—structured as dendritic fibers—affects their interaction with living cells. The hypothesis is that the intrinsic porosity of OMIECs can resemble the extracellular matrix and A portion of this thesis is therefore dedicated to developing an effective platform for this investigation, with the long-term goal of enabling direct *in-vitro* signal recording and stimulation. This approach may pave the way toward future applications involving the implantation of dendrite-based devices.
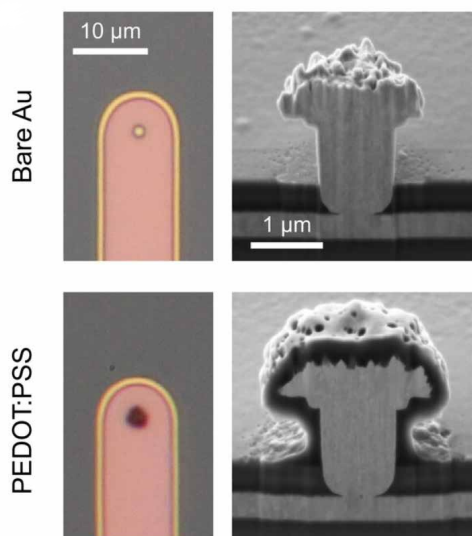
Figure 1.8: Example of bare and PEDOT-coated electrodes from the work of Jones *at al.*[2]. Optical and electron microscopy. Optical micrographs (left) and SEM of FIB cross-sections of bare (above) and PEDOT:PSS-coated (below) gold ultramicroelectrodes.

1.5.4 P3HT and photo-electrochemical cells (PEC)

P3HT properties

Poly(3-hexylthiophene) (P3HT) is a benchmark semiconducting polymer extensively employed in organic electronics due to its balanced charge transport, relatively low bandgap, and solution processability. Its chemical structure features a conjugated thiophene backbone with hexyl side chains, which enhance solubility and promote semi-crystalline ordering, while still mantaining a high porosity (Fig. 1.9). As for PEDOT, charge transport occurs through delocalized π-orbitals and the polymer morphology and crystallinity strongly influences charge mobility via intra- and inter-chain hopping mechanisms. In particular, regioregular P3HT (rr-P3HT) shows a high degree of order and π-π stacking, meaning that different chains tend to align their π-orbitals in more ordered structures, influencing the overall waveform of the delocalized electrons, thus its electronic and optical properties depending on the degree of critallinity[59,60,61], enhancing hole mobility up to 0.1 cm^2/Vs.

The property of most interest of P3HT is its optical absorption in the visible range, with a peak around 500–600 nm and an absorption edge close to 650 nm, aligning well with the solar spectrum. This property makes P3HT an ideal active layer in bulk heterojunction (BHJ) polymer solar cells (PSCs). One of the most studied blends for this application is P3HT:PCBM, in which [6,6]-phenyl-C_{61}-butyric acid methyl ester (PCBM) serves as the electron acceptor. Their combination leads to an efficient charge separation due to the LUMO offset and enables a complex interpenetrating network at the nanoscale that improves exciton dissociation and carrier collection[62].
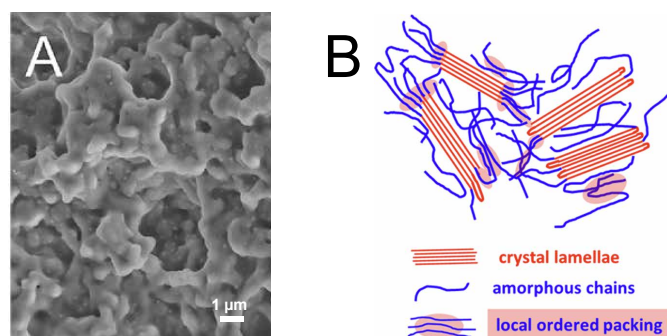
Figure 1.9: Characteristic morphology of bulk P3HT. (a) SEM image of electrodeposited P3HT, adapted from [31], (b) different organization of polymer chains in the material, with crystal lamellae, disodered chains and local ordered packing [63].

In this work we used instead P3HT:PF$_6$, which, even if it shares similar conductive and optical properties with those mentioned above, is not typically employed in solar cells, and not so present in literature. On the other hand, it represents a biocompatible material suitable for cellular interface and to be used in photo-electrochemical cells. It is also important to note that P3HT:PF$_6$ electropolymerization is possible, as demonstrated for instance in the studies of Ratcliff *et al.*[30]. Since it is a conductive polymer, the considerations previously made for PEDOT:PF$_6$ can be regarded as valid here as well, both in terms of doping behavior and its suitability for field-directed polymerization (FDP).

An interesting feature about P3HT is the evident difference between its oxidized and reduced form [64]. Indeed, the latter is red, poorly doped, optically sensible and less conductive than the former, blue and highly doped, but indifferent to light. In this way it is particularly easy to inspect its state along with the fabrication.

Unfortunately, as showed by Choi *et al.*[65] the release of PF$_6^-$ ions from the polymer is relatively easier than other dopants, leading to poor doping levels and low conductivity. However, the easier adoption of the same dopant for the PEDOT and P3HT backbones provides a solid basis for further optimization of the polymer with different dopants in future studies.

Photo-electrochemical cells

Beyond its application in solid-state photovoltaics, P3HT has emerged as a promising photoactive material in photoelectrochemical (PEC) systems. In particular many stydies demostrated the photocathodic properties of P3HT interfaced with acqueous solutions, which allow an effective charge separation and extraction, reducing the species present in the solution (mainly oxigen and hydrogen) [66,67,68,69,70].

When an exciton is generated in the bulk of the pure P3HT, charge separation can still happen through the π-stacking present in regioregular domains [59,71], and then the asymmetric carrier mobility between holes and electrons in the polymer allows holes to diffuse easily throughout the film, thus creating a space charge separation.

In the work of Chiaravalli *et al.*[71], PEC configurations are studied by depositing P3HT

films on transparent ITO electrodes, featuring a photovoltage under illumination. Here, an important role is given to dissolved oxygen in the electrolyte, which further hamper the mobility of electrons, trapping and extracting them in the solution, with generation of "super-oxide" (O_2^-. Upon light absorption, negative charges accumulate near the electrolyte interface and are extracted via reduction reactions with dissolved oxygen, leading to a measurable photovoltage. In Fig. 1.10 is shown a schematic representation of the interaction described above.
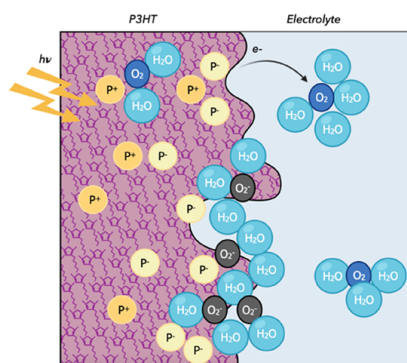
Figure 1.10: Faradic oxygen reaction at the P3HT/electrolyte interface. The oxigen in solution forms a complex P3HT$^+$:O_2^- hampering oxigen mobility. The so generated O_2^- charge is then screened by water molecules. Image adapded from [71].

CHAPTER 2

Materials and Methods

2.1 Device description

In order to perform field-directed polymerization, the device must feature two conductive electrodes with negligible thickness. Gold (Au) is the most commonly used material for this purpose. The choice of substrate depends on the application: in this case, since the device had to be tested under illumination and the available Arkeo setup (Cicci Research S.r.l.) only allowed bottom-side illumination, the substrate had to exhibit low absorbance. For this reason, glass was selected.

The electrodes were patterned via negative lithography, with an additional chromium (Cr) layer to enhance adhesion. The available mask featured devices with two electrodes separated by a gap of 15 to $3\,\mu$m. Since this spacing was too narrow to assess cell biocompatibility and fiber growth, we repurposed the square contact pads (Fig. 2.1, completely removing the micrometer-size gaps.

Figure 2.1: Miroscope image of the gold electrodes at the end of lithographic process on polyimide substrate.Measured distance between the electrodes.

Although the resulting electrode configuration was functional, it exhibited several non-idealities, primarily due to geometric constraints. The two electrodes were 1.5 mm square pads, resulting in a large exposed area in contact with the solution, which hindered polymerization not localized at the edges.

Moreover, the electrodes were spaced 1 mm apart—significantly larger than typical distances reported in the literature. However, Koizumi *et al.*[19] successfully obtained dendritic fibers at this distance. The main drawback of such a large spacing is the extended time and high voltages required for polymerization. This necessitated the addition of a chamber to contain the solution and minimize variability during the process. Additionally, the high voltages imposed the use of solvents with a compatible electrochemical window, such as acetonitrile, thus limiting the choice of dopants to those not requiring aqueous solutions. For this reason, the polymers were doped using tetrabutylammonium hexafluorophosphate (TBAPF$_6$), which dissolves well in acetonitrile.

For the second step it was necessary to develop a protocol to prevent cross-contamination between the two polymers during the two polymerization steps. In the case of P3HT as well, TBAPF$_6$ was used as the dopant. The presence of a chamber to contain the solution proved essential for performing deposition cyclic voltammetry. To facilitate this process, an Ag/AgCl reference electrode was added above the main contacts to serve as a reference for the potentiostat. However this electrode could not be used as gate for a OECT, considering the high variability between the devices.

Finally, the contact pads were enlarged to allow for proper connection to the fabrication instruments. This was achieved by attaching a strip of copper tape and electrically connecting it to the gold electrode using Ag/AgCl paste. A schematic representation of the device is shown in Fig. 2.2.

Most of experimental phase of this work was conducted at the Sensing Technologies Lab of the Free University of Bolzano. Cell viability experiments on the fabricated devices were carried out in collaboration with the Eurac Research Center.
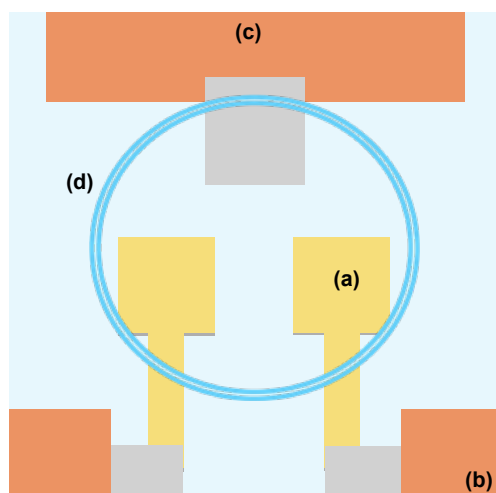
Figure 2.2: Schematic representation of the device. On the glss substrate: (a) gold electrodes, (b) copper tape contacts connected to gold with Ag/AgCl paste, (c) Ag/AgCl additional electrode as reference, (d) plastic ring as chamber.

2.2   Fabrication

Substrate preparation

Starting with common microscope glass slides, the substrates were pre-washed with glass soap, followed by sonication in acetone for 5 minutes, isopropanol for 5 minutes, and finally in deionized water for 5 minutes. The substrates were then dried using a nitrogen gun and stored in the cleanroom until use.

Microfabrication

The patterning of the design was achieved using negative photolithography. A pre-bake on a hotplate (Argo LAB M3-D) at 115°C for 5 minutes was performed first. Then, the substrates were treated for 5 minutes in a vapor beaker containing a few drops of hexamethyldisilazane (HMDS) to improve resist adhesion (Fig. 2.3a).

The resist used for this photolithography was MA-N 1420, a negative resist sensitive to UV light. The substrates were fixed in the spin coater (SPS Polos) using a vacuum pump. Then, 1 ml of resist was drop-cast from the center to the edge. The spinning routine was as follows: starting with an acceleration of 750 rpm/s up to 3000 rpm in 4 seconds, maintaining that speed for 30 seconds, followed by deceleration in 6 seconds, for a total of 40 seconds. This recipe yielded an approximately $2\,\mu$m-thick photoresist. Finally, a soft bake at 100°C for 2 minutes was used to remove the solvent from the resist.

a)   b)
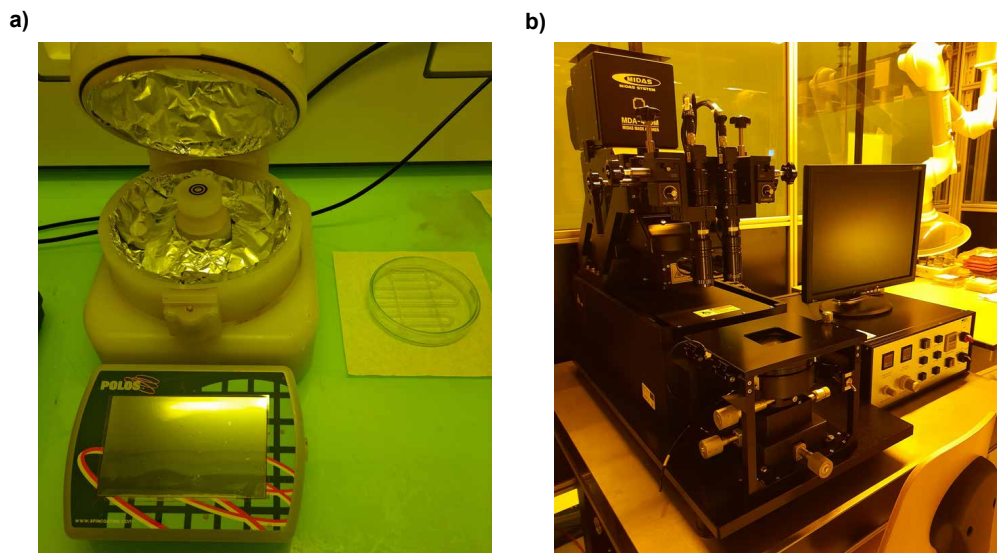
Figure 2.3: Some instruments used for lithography. In (a) spincoater (left) and beaker for HMDS pretreating (right). In (b) mask aligner setup from the outside of the cleanroom.

To define the pattern, the resist was exposed to UV light using a contact mask to select the exposed areas. The mask contains the desired pattern on a highly absorbing chromium layer, protecting the resist from exposure. In our case, the UV light induces cross-linking in the exposed regions, strongly reducing their solubility in the developer.

As a result, the negative of the mask is transferred to the resist, leaving holes and exposing the glass substrate in correspondence of the pattern. This step was performed using a mask aligner in cleanroom conditions (Fig. 2.3b).

The exposure time was calculated by dividing the required dose by the light intensity measured 30 minutes after the lamp was turned on, using a power meter. The required dose for the current procedure was $550\,\mathrm{mJ/cm^2}$:

$$\text{Exposure time [s]} = \frac{\text{Exposure dose [mJ/cm}^2]}{\text{Light intensity [mW/cm}^2]}$$

After exposure, the sample was immersed in approximately $200\,\mathrm{ml}$ of developer solution (MA-D 533/S) for 2.5 minutes, gently agitating the solution to ensure fresh developer contact. Then, the sample was rinsed in deionized water for 30 seconds and dried with a compressed air flow.

With the negative pattern defined in the resist, metallic contacts were deposited using a MBRAUN ProVap 5G thermal evaporator. First, $3\,\mathrm{nm}$ of chromium (Cr) were deposited as an adhesion layer, followed by $50\,\mathrm{nm}$ of gold (Au) for the electrodes.

After metal deposition, the lift-off process was performed to remove the resist and excess metal. The samples were immersed in a beaker with acetone for 45–60 minutes. If the previous steps were correctly executed, wrinkles appearead on the gold layer above parts where resist is still present (Fig. 2.4). The unwanted metal was then removed with sequential rinses in acetone, with the final step including 10 seconds of sonication. The samples were then dried using compressed air.
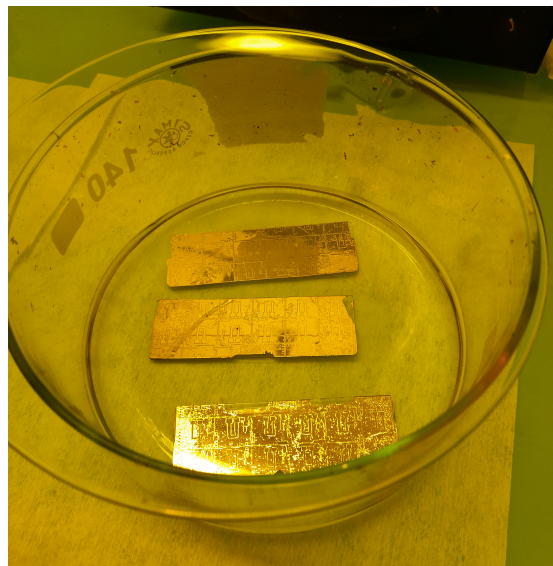
Figure 2.4: Samples after the evaporation set in acetone for 45-60 min for the lift-off. Here, first wrinkles appear on the samples after few minutes in solution.

Device assembly

The glass slides were cut into individual devices using a diamond pen and then fixed
again onto a glass slide with a transverse copper-tape stripe, grouping them in sets
of five. This step was needed both to group the samples by growth condition and to
facilitate later handling and analysis.

To facilitate electrical connection, a copper tape strip was also applied between the
samples, and the connection to the gold contacts was enhanced using Ag/AgCl paste.
Then a square of Ag/AgCl paste was also applied on the transverse copper-tape stripe,
to act as a non-polarizable electrode (e.i. reference electrode).

Finally, to contain the solution over the electrodes, a 7.5 mm-diameter ring cage was
glued and sealed over the sample using polydimethylsiloxane PDMS (Silkgard, 10:1 of
silicon elastomer and crosslinking agent, stored in the fridge). To accelerate PDMS
curing, the samples were heated at 150°C on a hotplate. Electrical interconnections were
verified at each step with a multimeter. The choice of this method to stick the chamber
was non-trivial: indeed such a adhesive layer has to be higly biocompatible and must
resist to acetonitrile attack, avoiding leakages. Many other glues have been tested before
optimizing this process.
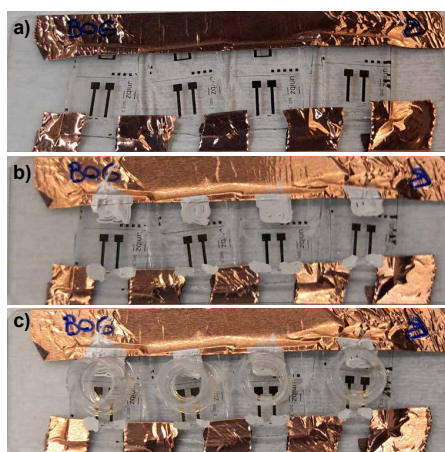
Figure 2.5: Step-by-step assembly of the devices. In (a) the samples after diamond-pen cutting
and taping on the supporting glass slide. In (b) Ag/AgCl paste is added on top as a supporting
reference during cyclic voltammetry. All the gates are connected to a common copper tape to
ease the connection in series. In (c) the rings are attached and sealed with PDMS.

Electro-polymerization

All electro-polymerization steps were conducted inside a glovebox (MBraun-ECO), main-
taining oxygen levels below 15 ppm. Although oxidation control is not strictly necessary
for PEDOT, it is important for cyclic voltammetry of P3HT. The complete setup was
then placed inside the glovebox and monitored live via a microscope camera connected
to a PC, as shown in Fig. 2.6.
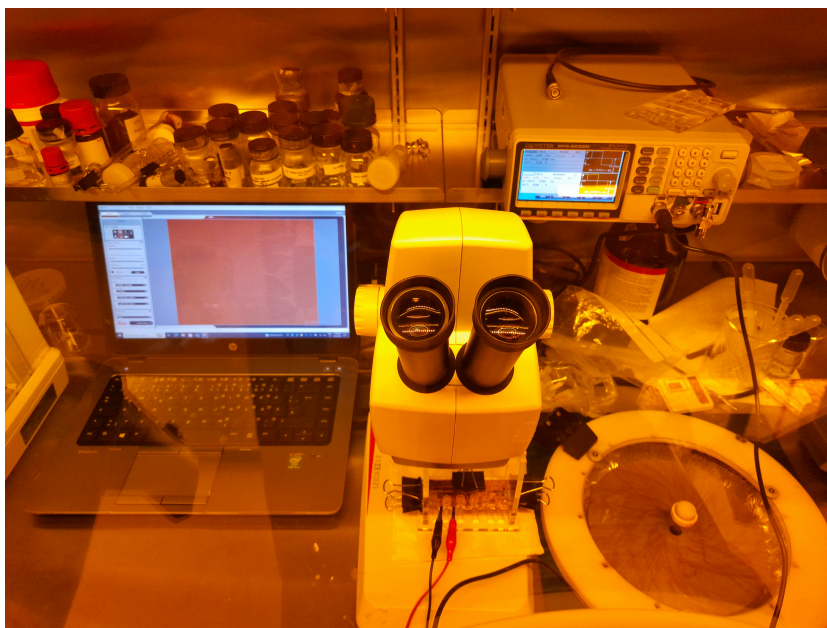
Figure 2.6: Electropolymerization setup inside the glovebox. On the right, the function generator ON and connected at CH1. In the middle the microscope mounting the camera. Under the microscope the custom PVC sample holder and a sample connected to the function generator. On the left, the computer used to acquire the videos and images.

The following solutions were then used for the electropolymerization:

- 50 mM EDOT (Sigma-Altrich) as monomer and 1 mM $TBAPF_6$ (Sigma-Altrich) as dopant in acetonitrile (for PEDOT)

- 50 mM 3HT (Sigma-Altrich) as monomer and 1 mM $TBAPF_6$ as dopant in acetonitrile (for P3HT)

All the solutions were stored in glovebox and left stirring on the hotplate for 20 minutes before use.

For AC-electropolymerization, the samples were placed on the custom sample holder shown in Fig. 2.6, then the chamber was filled with $100\,\mu$l of solution using a micropipette. The device contacts were the connected to a function generator (QW-INSTEK MFG-2230M) applying a square wave signal with amplitude ranging from 12 to 16 V peak-to-peak and fixed frequency 80 Hz. The formation of a conductive fiber was verified by the live images on the microscope and with a multimeter, measuring the resistance after disconnecting the function generator.

The fibers were then cleaned from residual solution, the chamber was rinsed by filling and emptying it twice with pure acetonitrile, and then dried at 60°C on the hotplate.

For the hybrid devices, P3HT was polymerized using cyclic voltammetry performed with a potentiostat (PalmSens4, USB/bluetooth battery powered potentiostat) in a three-electrode configuration: the two gold pads were short-circuited with a copper tape stripe and connected to the working electrode, the Ag/AgCl paste contact served as the refer-

ence, and a Pt wire was placed in the solution as the counter electrode. The CV range was between –1 V and +2 V, with a scan rate of 0.3 V/s. Approximately five cycles were sufficient to fully coat the PEDOT fibers, depending on their specific properties.

Washing and conditioning for cell deposition

To remove any residual of the solution, particularly important before cell deposition, the chamber was filled and emptied twice with acetonitrile, then immersed in fresh acetonitrile for 12 hours. The same procedure was repeated with isopropanol, this time with a 6-hour immersion. Finally, the fibers were stored in deionized water until cell deposition.

2.3 Characterization

2.3.1 Morphological characterization

Fiber images and fractal dimension

Almost all fiber images in this work were taken using the camera of a LeicaEZ 4E optical microscope during and after the polymerization. The characterization of fiber growth process was possible through fractal dimension analysis with the box counting method, conducted using ImageJ. The images were split into color channels, then the blue channel was binarized and processed using native tools within the software.

Surface analysis of the fibers was performed using the 3D surface profilometer Keyence VK-H3J (VK-3000 series) and analyzed with the relative software, selecting the whole surface of the fiber by color contrast with the glass substrate. The images were taken with both optical and lased mode with the 10x objective. The sample for this analysis was prepared from a pair of non-bridged fibers, electropolymerizing just one side, as shown in Sec. 3.2.

2.3.2 Electrical characterization

All resistance values were measured in dry conditions using a portable multimeter. Output characteristics and transfer characteristics of PEDOT fibers operating as OECTs were obtained with a probe station. This instrument presents up to four micro-manipulators (SMU) with gold needle probes connected to a Keysight B1500A semiconductor device parameter analyzer.
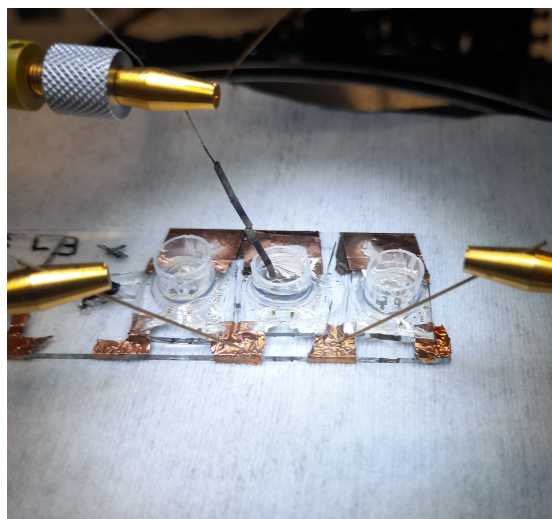
Figure 2.7: Sample under measurement at the probe station. Two gold needles connect to the electrodes as source and drain. An additional Ag/AgCl electrode is placed in the solution as gate contact.

To prevent short circuits from the copper tape with the base of the protestation a towel was placed below the sample. The position of the probes was monitored using a microscope mounted on the setup. The chamber was filled with 0.1 M PBS solution. Following the discussion made in Sec. 1.5.1, a top Ag/AgCl electrode (WPI) substituted one gold needle and was placed in the solution as the gate contact to ensure the highest gate capacitance, whereas the source and drain contacts were connected with gold needles, as in Fig. 2.7.

2.3.3   Optical characterization

Absorption measurements

An initial attempt was made to directly measure the absorption of PEDOT/P3HT fibers; however, this did not yield satisfactory results, as the fiber coverage over the substrate was minimal compared to the available aperture size. The absorption profile was therefore obtained a similar combination of the materials in a film. The analyzed sample was fabricated through cyclic voltammetry electropolymerization on a glass substrate coated with 100 nm of indium thin oxide (ITO) on glass. A plastic ring was placed on the ITO and filled with the monomer solution, after which a platinum counter electrode and an Ag/AgCl reference electrode were inserted from above. The ITO substrate was connected as the working electrode, improving the contact with a drop of Ag/AgCl paste.

Five cycles were performed using the PEDOT:PF_6 solution, after which the sample was rinsed with acetonitrile and left to dry. Subsequently, five additional cycles were run with the precursor solution for P3HT:PF_6. Both the cyclic voltammetry were executed using a voltage sweep between -1 V and $+2$ V at a scan rate of 0.3 V/s.

The absorption spectrum was acquired using UV-Vis spectroscopy with an Agilent 89089A spectrophotometer. A 6 mm diameter iris was placed over the sample to isolate the region of interest. As a blank, a glass/ITO substrate with the same iris configuration was used. The measurement was conducted over a wavelength range between 300 nm and 750 nm.

Photo-activity measurements

Before any photo-activity measurements, the fibers were left immersed overnight in phosphate buffered saline (PBS) to ensure electrochemical equilibrium was reached at the time of the measurement and minimize signal drift. All the optical measurements were peformed with Arkeo by Cicci Research. This instrument integrates two probes that allow to measure open-circuit voltage, short circuit voltage or to fix a voltage or a current between the probes. On the same time it is possible to control a 12-LED setup below the sample. The minimum response time of the LED is 500 ms, so the highest achievable frequency is 2 Hz. The power intensity is displayed on a scale from 0 to 255, and a minimum threshold is required to activate the LED depending on its specific type. Since no information about the irradiance is provided, all results in this work are expressed as a percentage of the maximum emitted power.
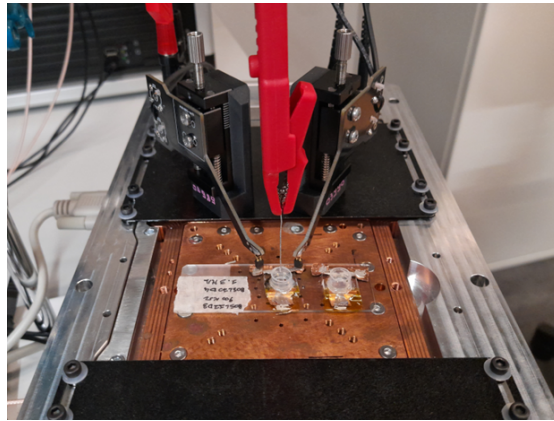
Figure 2.8: Setup of the electrodes used to measure the vertical and horizontal voltages. The red crimp holds the platinum wire in solution and is connected to the positive pole of the machine. The other probes are always on the sample but for vertical measurements a copper tape is placed below them to short the contacts and the positive pole one is disconnected.

Both the wavelength dependence and the power intensity dependence of the photovoltage were investigated. For the former, the LED power was set at 30% of the maximum intensity, using different LED colors. For the latter, the cold-white LED was employed, with power levels ranging from 12% to 100% in steps of 12%.

Throughout this study, two types of measurements were considered: "horizontal" measurements, performed between the two gold contacts using the native probes of the Arkeo system, and "vertical" measurements, carried out by inserting a platinum wire electrode from the top into the solution and shorting the two gold contacts using copper tape, then connected with the probe to the negative pole of the machine.

2.3.4 Cell viability assesment

Human neuroblastoma cells (SH-SY5Y, ATCC CRL-2266 – Cell Bank – IRCCS AOU San Martino IST) were cloned from a bone marrow biopsy derived line called SK-N-S, taken from a four-year old female with neuroblastoma. This cell line is often used as in vitro model of neuronal function and differentiation. This line was cultured in DMEM-F12 (Thermo fisher Scientific #11320033) medium supplemented with 10% FBS (Sigma-Aldrich) and 1% penicillin-streptomycin (Biowest #L0022-100). When the cell culture becomes confluent (around 80/90%) it is moved with a lower confluence in a different petri dish. The culture is washed with Dulbecco´s phosphate buffered saline (PBS Biowest #L0615-500), then incubated at 37° and $CO2$ 5% for 5 minutes with 0,05% trypsin in EDTA (Gibco #25300-054). After the incubation, the action of the trypsin is stopped by using a pre-warmed medium and the cell culture is replated at the preferred confluence. The biocompatibility of the fibers was assessed by analyzing the morphology of the cells adhered to their surface. In fact, the loss of cellular viability is typically associated with a change in morphology, as dead or dying cells tend to lose their typical elongated or spread shape, becoming rounded or spherical.

CHAPTER 3

Results

3.1 PEDOT:PF$_6$ and P3HT:PF$_6$ fibers

Field directed polymerization of PEDOT:PF$_6$

The goal of our fiber fabrication using field-directed polymerization (FDP) was to obtain a sufficiently conductive interconnection between the electrodes while preserving characteristic morphological features such as strong branching and directionality aligned with the applied electric field. These traits are also relevant to our aim of testing the interaction between dendritic fiber morphologies and *in-vitro* cell cultures.

Despite several limitations, the advantage of working with a large electrode gap allowed to directly observe a slower growth, an essential factor in identifying optimal polymerization parameters. In Fig. 3.1 below are shown selected frames from real-time growth, enabling analysis of the evolution described above.
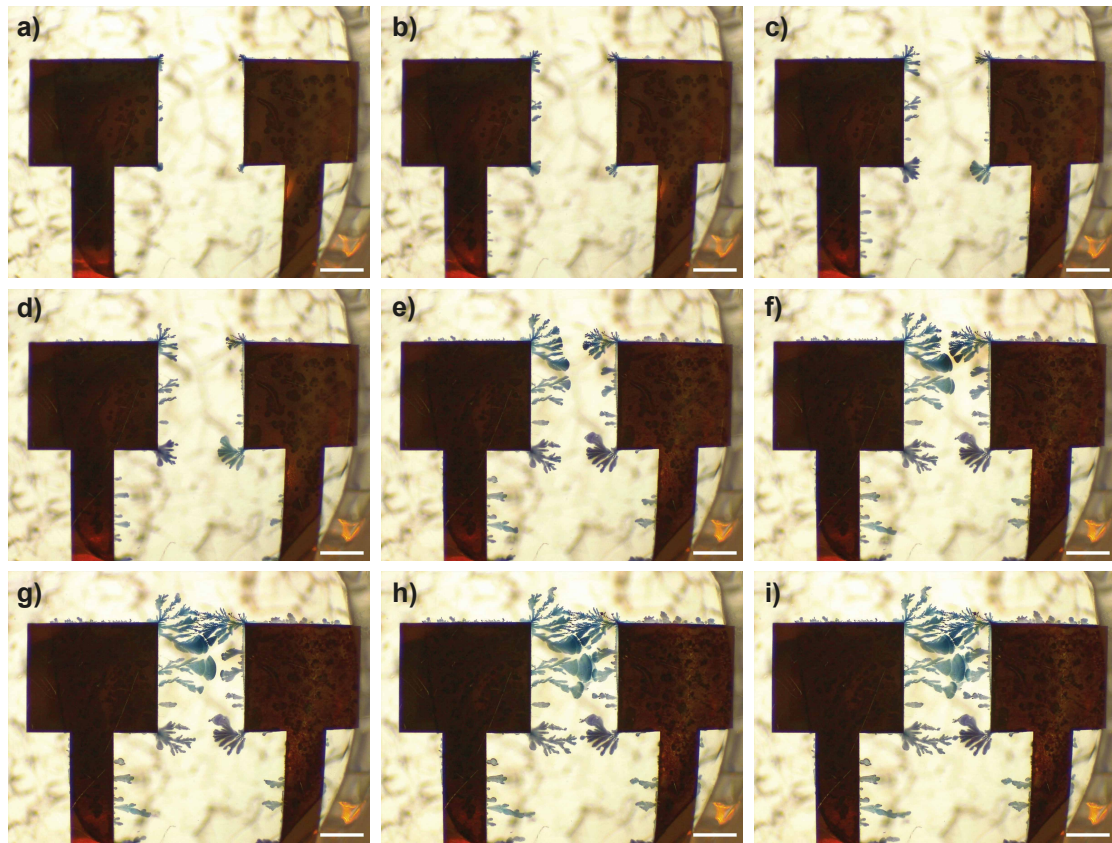
Figure 3.1: Selected frames of PEDOT-fibers growing

In Fig. 3.1a, we observe that polymerization starts from the electrode corners, where the electric field is stronger and ion dynamics is therefore faster. Once an initial tip forms, the fiber begins to branch. This is made possible by the use of moderately high frequency (80 Hz) and a relatively low starting voltage (12 V peak-to-peak), which allows the electric field to be sufficiently strong at multiple sites across the electrode, but enough to restrain the polymerization to a single point. In such conditions, more than one "discrete" location can exceed the polymerization threshold simultaneously, resulting

in spatially distributed initiation points. In some terms, this can correspond to field lines diverging from a common origin, spreading into multiple directions.

Starting at lower voltages also provides protection against contact damage. Once a tip is formed, it becomes favored by the electric field over the gold electrode itself. Gradually increasing the voltage has proven effective in preventing contact erosion, while also being necessary to sustain practical growth times. Once a stable branching base is established (Fig. 3.1b), a progressive voltage increase enables faster growth without significantly altering the initial topology, producing fibers that expand from their nucleation center (Fig. 3.1c). Over time, new fibers become relevant on the side of the electrode, especially as the applied voltage increases and the field becomes sufficiently strong in those areas (Fig. 3.1d).

The reaction proceeds until two fibers meet and form a connection (Fig. 3.1f). Being PEDOT:PF$_6$ considered a sufficiently conductive material, we should expect the growth to stop abruptly upon contact. However, as reported in previous studies[6,19], polymerization continues beyond the initial bridging phase, reinforcing the connection until reaching saturation. Moreover, given the relatively large distances involved, the resistivity of PEDOT:PF$_6$ is not low enough to suppress the voltage drop across the electrodes entirely. Polymerization speed slows down and stops at the point of contact, continuing elsewhere (Fig. 3.1g). This process persists until the resistance between the electrodes drops to a level where polymerization becomes extremely slow or ceases entirely, forming a low-resistance connection (Fig. 3.1i).
An empirical method to establish if the connection is conductive enough relies on the observation of traces of contact damage caused by the passage of excessive current, which produces a result similar to the one presented in 2, also accompanied by bubble formation. This is likely due to local heating resulting from Joule effect.

Although this type of branched growth was frequently observed, alternative dynamics also occurred under identical experimental conditions. In some instances, no branching was present, and the polymerization proceeded uniformly along a kind of a wavefront (*Fig. 3.2*). This behavior appeared to be random and uncontrollable. Although it can produce large fibers and reduced resistance, the loss of branching makes the result more akin to a film—far from the intended goal of this study. Notably, this behavior could sometimes be suppressed by increasing the frequency or lowering the applied voltage, though not always effectively.

A possible explanation relates to the balance between electric field strength and diffusion: field driven aggregation should lead to high, field-directed branching, whereas diffusion effects happen almost isotopically. The concurrence of these two phenomena gives rise to this semicircular blooming rather than localized branching.

Another useful observation made possible by this setup is the visible color change when a signal is applied to a disconnected fiber. It is well known from literature the variation of color of PEDOT-based materials depending on its oxidation[72]. Initially, fibers appear dark blue, but upon applying the signal,the color lightens. This is consistent with previous observations on PEDOT: in its highly doped and oxidized state, the material takes
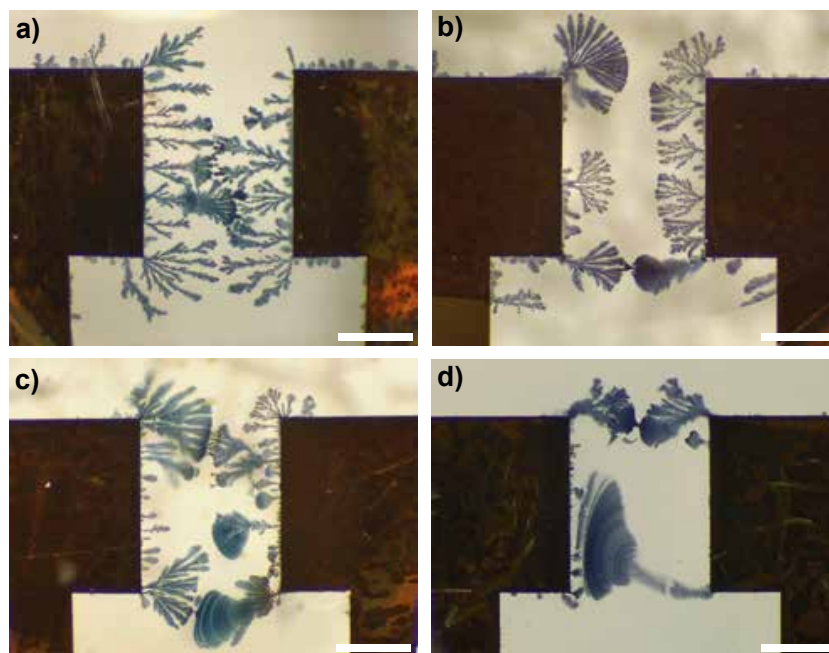
Figure 3.2: Examples of results of AC-electro-polymerization with PEDOT:PF$_6$. In (a) and (b)fibers from more regular field directed polymerization, whereas in (c) and (d) strong "blooming" effect present. Scalebar is 500μm.

on a pale blue color[72,73]. The reason why the fibers do not undergo full dedoping during the negative half-cycle is that the ions—trapped within the polymer matrix as a result of their involvement in the polymerization—cannot respond rapidly enough to the 80 Hz signal and thus accumulate within the fiber, temporarily increasing its conductivity. When the signal is turned off, some of the dopant is released and the doping level drops, partially reducing the fiber's conductivity.

This same observation also revealed that polymerization does not proceed uniformly along a given fiber. Instead, growth speed may shift between different fibers over time, depending on the distribution of the electric field. This is evident from subtle color variations across the fiber network. Occasionally, a fiber was seen to disconnect from the electrode entirely, turning a deep blue—indicative of a highly reduced state. Such fibers were found to be non-conductive and did not support further polymerization (*Fig. 3.3*. However, when the connection was re-established, possibly by chance, the fiber regained conductivity and growth was resumed.

These results demonstrate the possibility of reactivating a disconnected fiber simply by re-immersing it in solution and restoring doping conditions with an applied signal, namely forcing an electrochemical doping, enabling reinforcement or even "healing" properties. Anyway, after polymerization the fiber undergoes structural and chemical small changes, potentially altering the dopant concentration or reorganizing the polymer matrix. This mainly results in modifications of the electrical properties that are difficult to control or inspect, especially in such a large polymer volume. This issue proved to be particularly challenging in achieving reproducibly conductive fibers, as will be discussed in Sec 3.4.
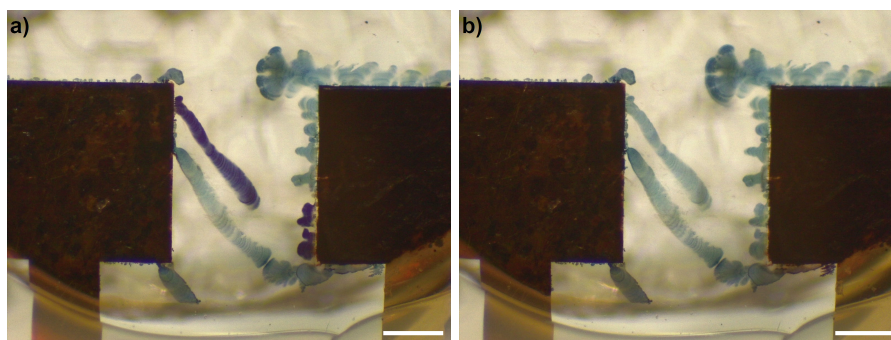
Figure 3.3: Example of PEDOT:PF$_6$ change in doping during polymerization. In picture (a) a fiber gets disconnected from the contact and the ions are removed, making it dark blue and stopping polymerization. In picture (b) the fibers gets connected again as the polymerization goes on in the solution, and its oxidation and conductivity is restored. Scale bar: 500µm.

Field-directed polymerization of P3HT:PF$_6$

Building on the experiments performed with PEDOT:PF$_6$ and starting from the assumption that FDP can be applied to different monomer-dopant pairs, we attempted to synthesize fibers of P3HT:PF$_6$. Using the same dopant allows us to retain all considerations related to its transport dynamics in solution as a function of the applied signal, as well as previously discussed observations regarding contact erosion. However, the differences in the way the monomer diffuses toward the polymerization site during growth, and how it subsequently organizes, becomes critical in determining the resulting fiber morphology. Polymerization using the same parameters as those for PEDOT:PF$_6$ yielded promising results. Figure 3.4 shows frame-by-frame growth of a P3HT:PF$_6$ fiber at 80,Hz and fixed 7,V.

Compared to PEDOT:PF$_6$, before any fiber branches out, multiple polymerization sites appear across the electrode surface (Fig. 3.4a); one of them eventually gives rise to a growing fiber (Fig. 3.4c). At this stage the polymer is very dark blue, nearly black, indicating an oxidized and thus doped and thus conductive state, which explains the progression of polymerization.

P3HT:PF$_6$ fibers appear more compact, with less branching and more localized growth. Branching occurs through clean, well-defined bifurcations (Fig. 3.4d). Unlike PEDOT:PF$_6$, growth does not necessarily begin at the electrode corners, but rather from a previously polymerized site. This observation may align with studies on P3HT film formation via cyclic voltammetry[31], which highlight the importance of uniform initial nucleation for homogeneous coverage. In our case, nucleation appears random, and the large electrode area introduces considerable variability across samples.

The resulting fibers tend to be thick, and polymerization occurs faster than with PEDOT:PF$_6$. Additionally, polymerization remains highly localized at regions where polymer already exists, with a lower number of new branched out fibers. Once one site of the electrode dominates, FDP proceeds from that point and almost ceases elsewhere. These fibers are also more flexible, plastic, and three-dimensional, moving freely in solution—driven by
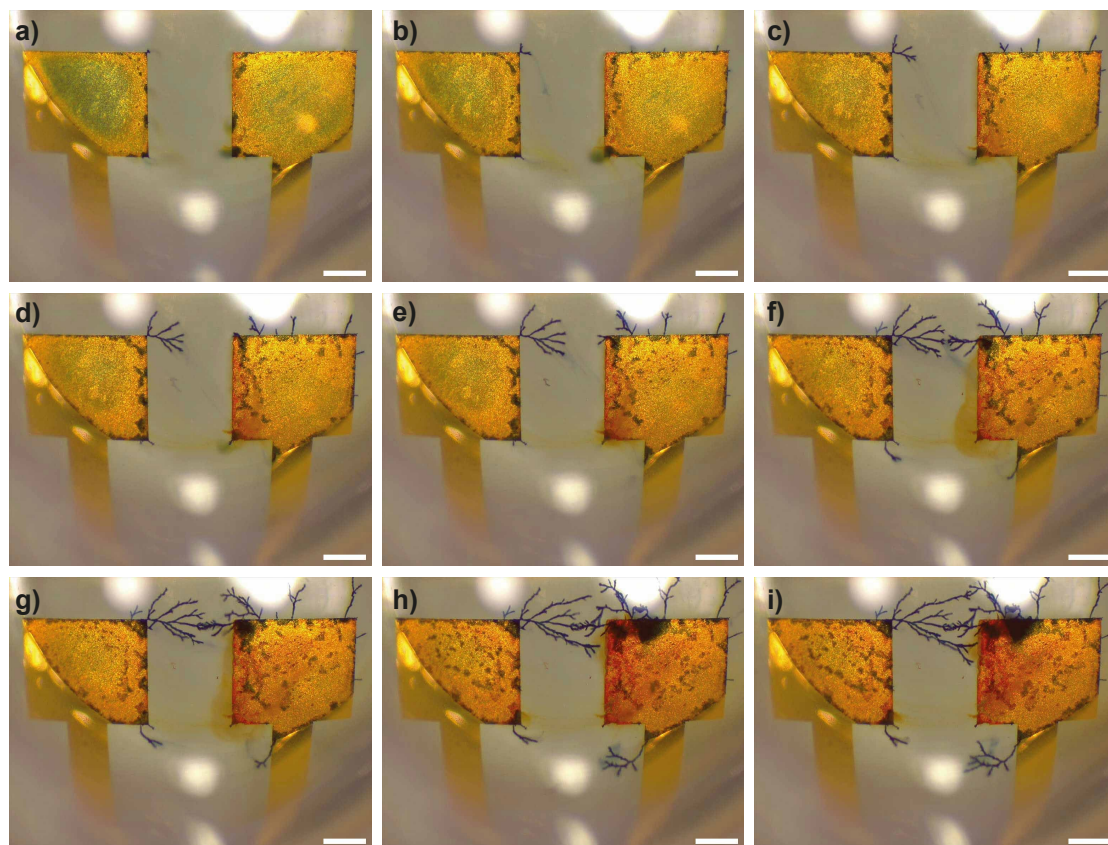
Figure 3.4: Selected frames form FDP of P3HT. From (a) to (c), initial nucleation and branching. From (d) to (f) fiber growth and bridging. From (g) to (i) strengthening of the connection and polymerization of the gold contact. Scale bar: 500µm.

the field both in terms of polymerization and mechanical movement, as if being pulled by the field itself. In some cases the fibers start vibrating under the effect of the salt drift. When two fibers bridge two electrodes, polymerization expands over the electrode surface (Fig. 3.4f). As observed with PEDOT:PF$_6$, the process continues beyond bridging, eventually reaching saturation. At this point, turning off the signal results in an unexpected phenomenon: the fiber begins to contract and changes color, becoming increasingly red—indicative of a reduced state. Fibers stretched between electrodes become weak and sometimes even break, as shown in Figure 3.5, losing the original topology. It is important to specify that this occurs when the fiber is still in the solution and within 30 seconds after the interruption of the signal.

If the signal is re-applied, the fiber swells again and regains the bluish color of its oxidized, conductive state. Applying a low-frequency signal revealed clear mechanical contraction and expansion of the fiber. Two hypotheses may explain this behavior. First, considering that conductivity in P3HT is mediated by polarons—as described in the introduction—the formation of a polaron is accompanied by a distortion of the polymer chain. As observed in electrochemical doping studies[65], PF$_6^-$ does not induce a strong, irreversible doping, as it is relatively easy to remove from an energetic standpoint. Therefore, while the ion dynamics at 80,Hz may not be fast enough to dedope the fiber during
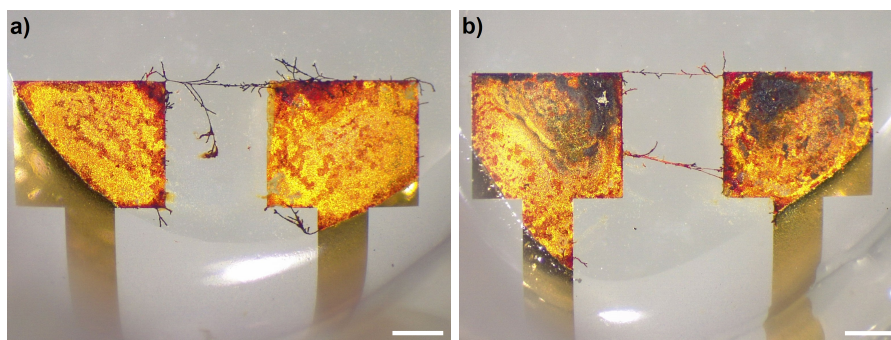
Figure 3.5: Examples of P3HT fibers after signal interruption and in dry conditions. The first sample (a) is the one displayed in 3.4. In (b) highly stretched fibers, also from polymerization sites different than the corners. Scale bar is 500µm.

the negative half-cycle, when the signal is turned off, more dopant diffuses out over time, leading to the observed contraction.

Since our goal is to use P3HT fibers for photostimulation, having the material in a reduced state is essential for generating a photovoltage. However, very low doping levels also reduce charge transport capacity, making the fibers functionally unsuitable.

The change in the dominant polymerization site—previously observed in PEDOT—was also seen in P3HT. The difference is that PEDOT fibers remain mechanically stable, whereas P3HT fibers contract and, if not connected at both ends, tend to collapse entirely, as seen in Figure 3.6, where the first fiber "switches-off" and a second one starts branching out. Although intense potentials at low frequency can re-oxidize and recover the fiber, this practice is discouraged due to the risk of damaging the gold contacts. Moreover this phenomenon is completely randomic and causes low yield of interconnected contacts

A second explanation for this contraction lies in the known tendency of P3HT to form regio-regular domains that reassemble after polymerization[59], likely causing shrinkage. High regioregularity is critical for both electronic transport[60,74] and photostimulation[71,75], since charge separation occurs within the $\pi-$stacking. Fibers stretched across electrodes may also prevent the polymer from settling into its optimal conformation, further hindering photostimulation performance.

In conclusion, P3HT fibers showed low mechanical stability, poor retention of the shape acquired during polymerization, and insufficient conductivity. It is important to note that these results were obtained over large electrode gaps, where contact erosion limited the ability to experiment with increased dopant concentration.
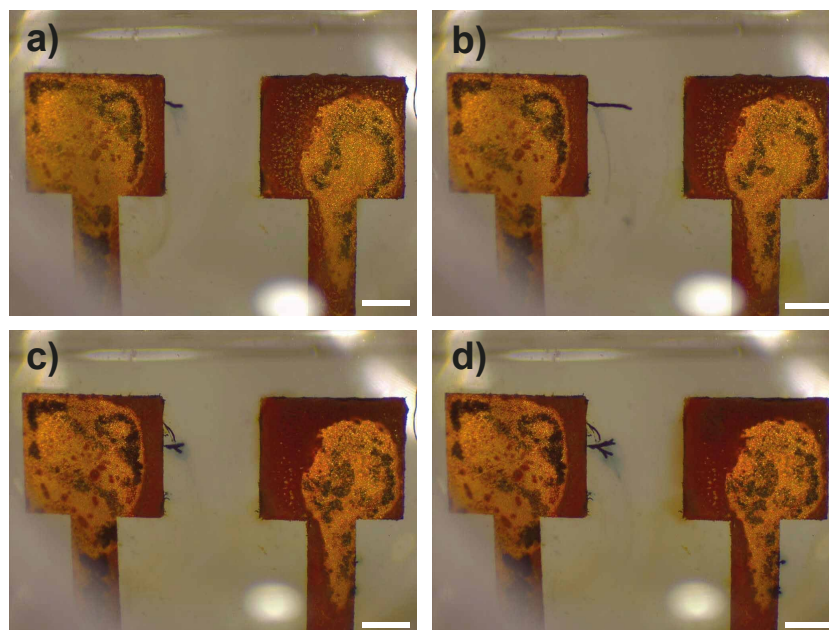
Figure 3.6: Example of suppression of branched out fiber in P3HT Ac-electropolymerization. In (a) and (b), fiber initially branches out from the middle of the electrode. In (c), for unknown reasons it gets disconnected, losing all the dopant, losing its structure. Another fiber branches out and starts growing from a nearby site (d).

3.2 Hybrid PEDOT:PF$_6$/P3HT:PF$_6$ fibers

Given the poor performance of P3HT:PF$_6$ fibers in this long-distance configuration, we explored the possibility of functionalizing the reliable platform provided by PEDOT:PF$_6$ fibers—whose polymerization was well-established—as a hole transport layer by depositing a film of P3HT via electropolymerization through cyclic voltammetry.

Figure 3.7 shows the PEDOT fiber during CV cycles. In this example, the electrodes are not bridged by the fibers and only one is connected to the working electrode, while the other acts as a reference.

When the signal reaches the peak oxidative potential of PEDOT, the fiber becomes oxidized (Fig. 3.7a), turning light blue. After this point, the monomer 3HT also oxidizes, initiating polymerization, coating the fibers with darker blue oxidized P3HT. During the reverse scan, the polymer is reduced, visible by the P3HT turning red (Fig. 3.7b). From Fig. 3.7c to Fig. 3.7h it is possible to observe the evolution of the film thickness with the scan. An indicative estimation of the coating can be made thanks to the electrochromic properties of P3HT, that allows to observe directly the degree of polymerization on the fiber during the oxidative phase. With our polymerization parameters, multiple cycles were needed to reach the final coverage shown in Fig. 3.7h.
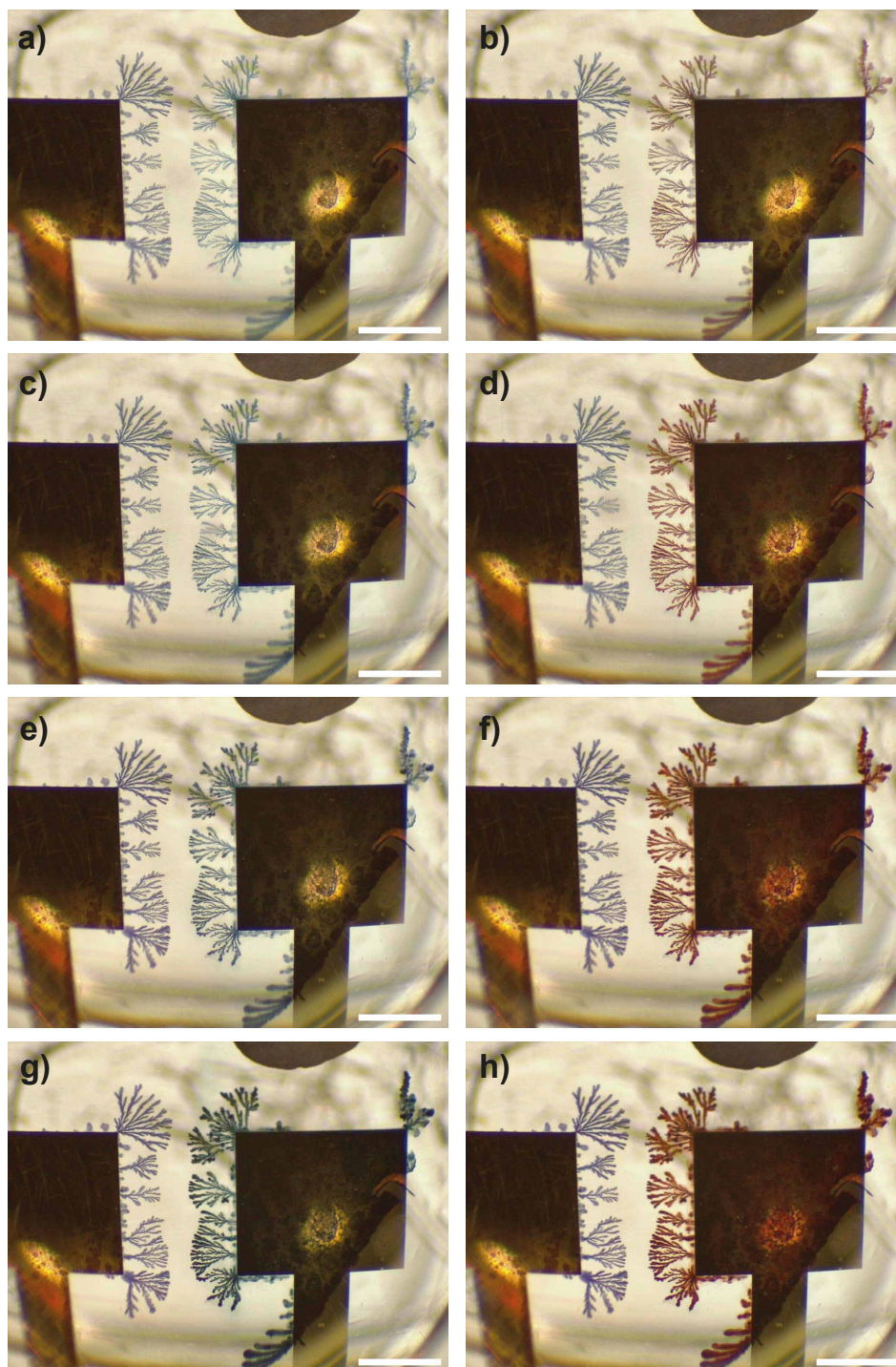
Figure 3.7: Evolution of the fiber along polymerization with cyclic voltammetry. In this sample only the right side electrode has been connected and the left side serves as a reference to PEDOT. The images (a), (c), (d) and (g) correspond to the oxidated state, whereas (b),(d),(f) and (h) correspond to the reduced state. From top to bottom, increase of the P3HT thickness can be observed by the increasing contrast color. (h) also corresponds to the final result at the end of the process.

One major advantages of using a potentiostat for electropolymerization is the ability to monitor the current during the process, producing voltammograms. Although the configuration used here is not ideal for quantitative CV analysis, qualitative observations are still meaningful.

Figure 3.8 shows an example voltammogram of a PEDOT/P3HT coating over the first cycle. In the oxidative scan, an initial oxidative peak appears, likely corresponding to the oxidation of PEDOT:PF_6. Following that, a sharp increase in current is seen—typically associated with irreversible chemical reactions at the working electrode. In our case, this corresponds to the onset of monomer oxidation and polymerization. In the reverse scan, as expected from this kind of transformation, the characteristic PEDOT peak is almost absent, having been covered by a thin P3HT layer. Nonetheless, a residual signal is detectable. The distance between those redox peaks is approximately 80 mV, indicative of a quasi-irreversible reaction, probably related to doping and dedoping of PEDOT:PF_6.
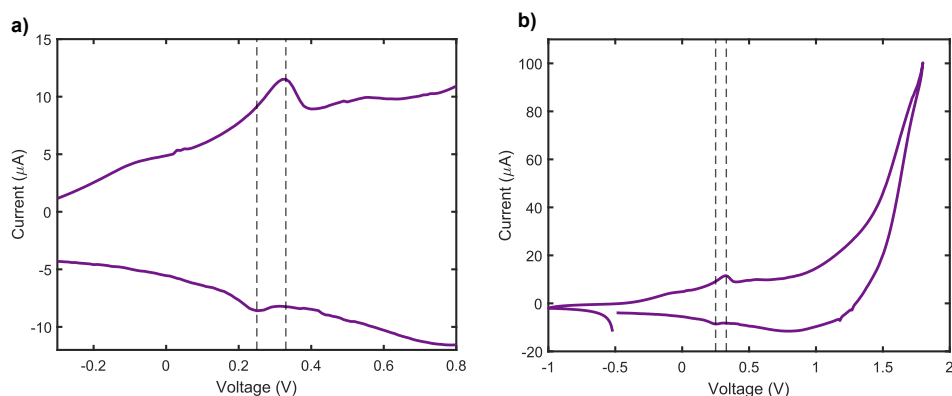
Figure 3.8: First cycle of PEDOT/P3HT coating (b) and detail over the residual oxidative and reductive peaks (a) of PEDOT:PF_6. Vertical lines corresponding to the position of the peaks. The measured separatio between the peaks is 80mV that should correspond to a reversible redox reaction, related to PEDOT:PF_6 doping.

As the film grows in the following scans, currents increase with each layer of added P3HT (*Fig. 3.9*). Additional peaks emerge in both the oxidative and reductive sweeps, while those related to PEDOT vanish. The oxidative peak splits into two overlapping peaks, a phenomenon also observed in prior studies on P3HT doping[65], attributed to the coexistence of crystalline and amorphous regions in the polymer.
Since exciton separation in P3HT occurs primarily in the crystalline regions, where π-stacking is prominent—as discussed in Sec. 1.5.4, observing such features during fabrication is important for photostimulation applications.

Since this CV process involves polymerization at the working electrode, further considerations regarding peak positions are limited: peak shape and amplitude vary with the amount of polymer present, a condition not recommended in any CV measurement.
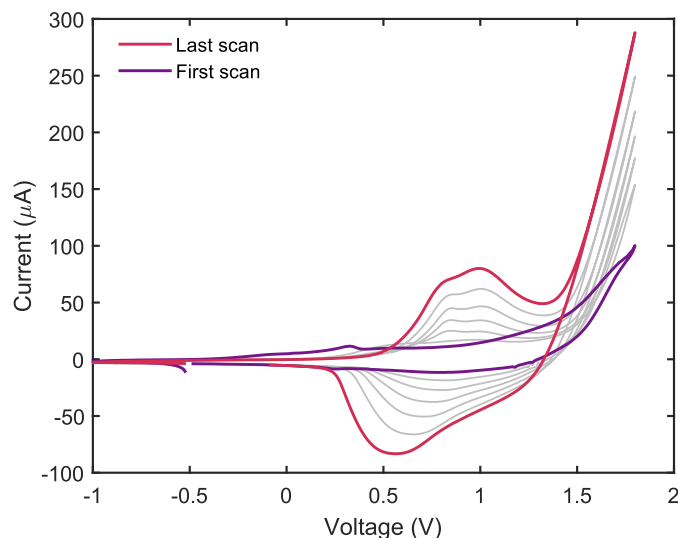
Figure 3.9: Overlay of the voltammograms corresponding to the sample in Fig. 3.7. With respect to the first scan (purple curve) the following scans increase in current and present characteristic redox peaks. The peaks in the reduction scan present a shift due to the polymerization at the electrode surface. In the last scan (magenta curve), the oxidation peak evidences two convoluted peaks related to the crystalline and amorphous energy levels.

The cyclic voltammetry protocol showed a good repeatability among most of the samples, especially when the two contacts were short-circuited. Some examples of the obtained devices are reported in figure 3.10.
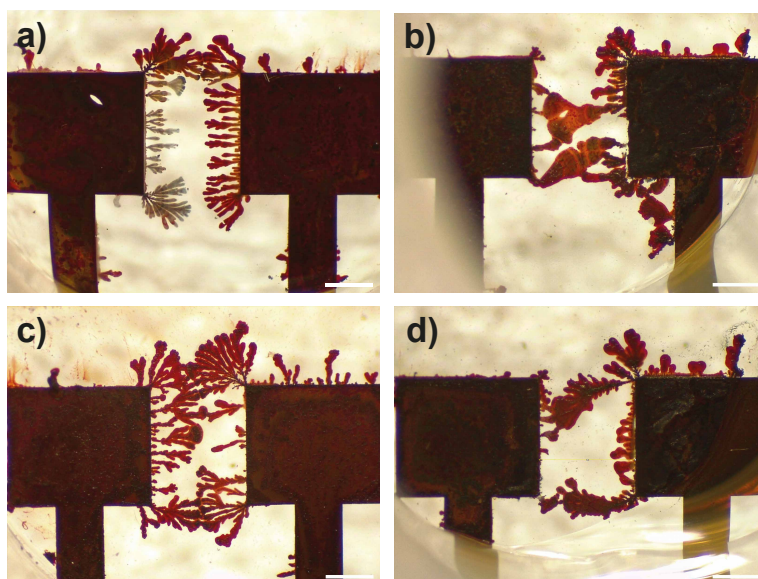
Figure 3.10: Some examples of P3HT coated PEDOT fibers. In figure (a) a sample obtained without shorting the contacts presents some lowly covered surface. Samples in figures (b), (c) and (d) are obtained shorting the contacts, leading to a more uniform coverage.

3.3   Morphological characterization

Fractal analysis

Studying the morphology of fibers obtained through AC electropolymerization, it is important to consider the two competing mechanisms that drive growth: the drift of salt ions induced by the applied electric field, and diffusion phenomena resulting from concentration gradients formed during the reaction. In particular, the other competing mechanism to FDP is indeed Diffusion-Limited Aggregation (DLA), as already reported by Koizumi *et al.*[19]. Both mechanisms operate simultaneously, though their relative influence depends on the specific experimental conditions.

To assess the extent to which PEDOT fibers are influenced by drift versus diffusion, the fractal dimension was calculated using the box-counting method[76]. For DLA-type growth, this dimension typically approaches 1.71. Figure 3.11 shows the distribution of fractal dimension values calculated for PEDOT and P3HT fibers.
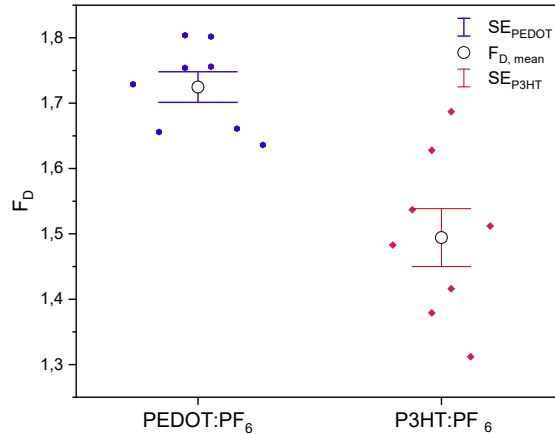
Figure 3.11: Distribution of the results of the fractal analysis of the fibers grown through AC-electropolymerization with corresponding standard error and mean value. In blue the the values for PEDOT:PF_6 and in red the values for P3HT:PF_6.

The average F_D value obtained for PEDOT was 1.73, which is consistent with a DLA behavior. This was an unexpected result, but we must consider that many samples exhibited a F_D lower than 1.71. We must consider that since the analysis was conducted on the full image of a fiber grown along the electrode edge, there may be different kinds of fibers branching out.

Indeed, some fibers or fiber segments exhibited particularly low fractal dimension values, while others showed significantly higher values. The latter correspond to the "blooming" fibers discussed in the previous in Sec. 3.1, confirming that these result from diffusion-dominated mechanisms rather than field-driven growth.

This behavior, more clearly observed over longer distances, can be interpreted as follows: when the field is low and the frequency is high, diffusion does not limit polymerization, which occurs mainly at points reached by the speed of ionic drift. The growth is thus

more localized. When the field increases excessively, polymerization consumes monomers more rapidly and their diffusion limits the polymerization, while the typical field limited aggregation features disappear. This gives rise to "waves" driven by precursor diffusion near the active polymerization site.

In contrast, P3HT:PF$_6$ fibers exhibit a lower fractal dimension, with an average of 1.49. This outcome aligns with prior observations: P3HT:PF$_6$ fibers, grown under the conditions described, show less branching and appear more thread-like and rectilinear. It can therefore be concluded that the polymerization of P3HT:PF$_6$ is primarily field-driven, with diffusion playing a less significant role.

Nevertheless, P3HT:PF$_6$ fibers also display greater variance in their fractal dimension compared to PEDOT. These fibers grow faster, and in some cases, exhibit virtually no branching, resulting in very low F_D values. This confirms the earlier observation that P3HT:PF$_6$ fibers are more tightly linked to electric field effects.

Confocal microscope and 3D profile

In Figure 3.12 the images from confocal microscope and related, height profiles are shown. The morphology of both PEDOT and PEDOT/P3HT fibers appears highly irregular, making punctual step height study unfeasible. By combining optical and laser images from the confocal microscope, it was possible to extract 3D surface profiles of selected samples (see figures), which were then analyzed in terms of roughness and material height distribution.

The results of the analysis are displayed in 3.1. The first parameter to note is the arithmetic mean height (Sa), which appears very low for both samples within the analyzed area, especially when compared to their respective maximum peak height. This suggests the presence of large voids between morphological features, which reduces the mean value. It should also be considered that these measurements were taken after complete drying of the samples, and PEDOT is known to shrink up to 60% of its volume in dry conditions compared to the original volume after polymerization in liquid.

Focusing again on Sa, the difference between the two samples is 600µm, which can be interpreted as the average coating thickness. However, if the maximum peak height (Sp) is taken into account, the observed peak difference of approximately 2 µm may serve as an estimate of the maximum coating thickness. Since polymerization is more likely to occur at edges, tips, or peaks, this value provides a more representative upper limit to the film thickness.

Another relevant observation—especially considering the operation in electrolyte—is the sharp increase of the developed interfacial area (Sdr) after the P3HT coating. This indicates that the coating does not flatten the fiber profile, but instead increases its active surface area, maintaining the roughness. This result is particularly important for this study, since the fibers are in contact with the electrolyte and involved in electrochemical reactions, where interfacial surface plays a crucial role in mechanisms such as doping and extraction of photo-generated electrons, as discussed in Sec. 1.5.4.
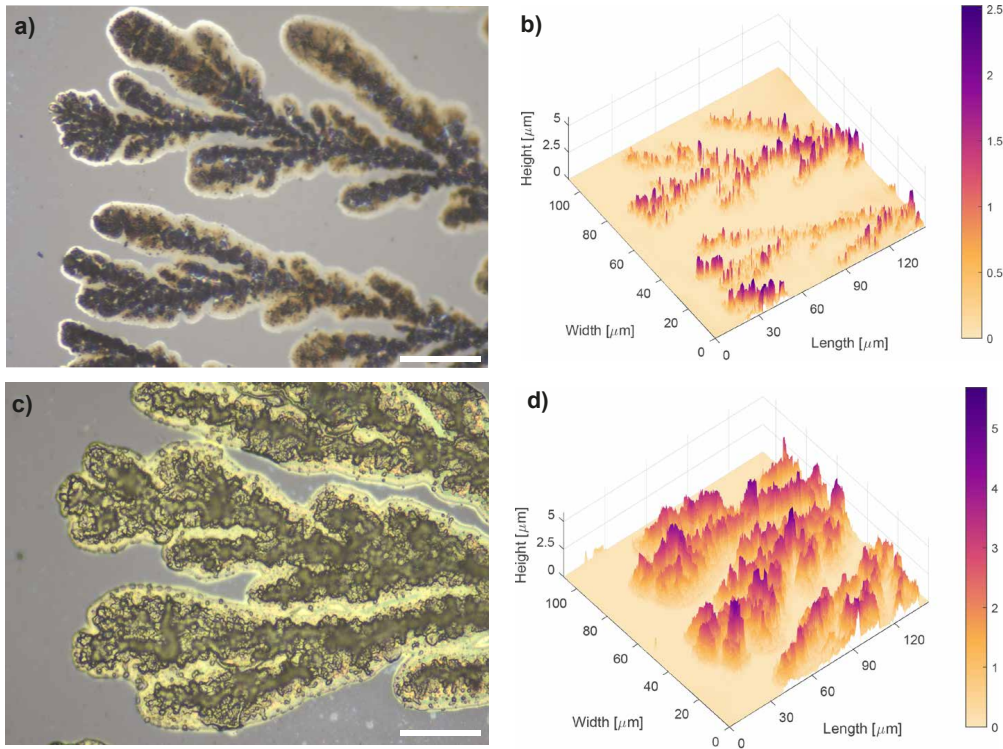
Figure 3.12: Results from the 3D profilometer and confocal microscope. In (a) and (b) respectively the image from confocal microscope and the 3D profile extracted for PEDOT fibers. In (c) and (d) images from confocal microscope and the 3D-profile extracted for PEDOT/P3HT fibers.

Finally, the PEDOT sample shows a high and positive skewness (S_{sk}), meaning that the height distribution of the surface profile is asymmetrical with a longer tail on the right, i.e., dominated by protrusions rather than depressions. The kurtosis (S_{ku}) is also significantly above 3, indicating a leptokurtic distribution characterized by a high concentration of values around the mean and the presence of isolated sharp features. In contrast, the PEDOT/P3HT sample presents more moderate values of both parameters—still suggesting a peak-dominated morphology, though less extreme and with more uniformly distributed features. The arithmetic mean peak curvature (S_{pc}), which describes the sharpness of the highest surface asperities, is also remarkably high, exceeding 9000, indicating steep and narrow peaks. It can therefore be assumed that the P3HT coating induces a general smoothing between the peaks, while still increasing the overall surface roughness.

Material	S_a (µm)	S_p (µm)	S_{pc} (1/mm)	S_{dr}	S_{sk}	S_{ku}
PEDOT	0.231	2.291	5144.028	0.3188	2.433	10.180
PEDOT/P3HT	0.804	4.485	9205.069	0.5599	0.819	2.973

Table 3.1: Data extracted from the analysis obtained with confocal microscope on the area selected as described in Sec. 2.3.1. Roughness parameters from confocal surface analysis. S_a = Arithmetical mean height; S_z = Maximum height; S_{pc} = Arithmetic mean peak curvature; S_{dr} = Developed interfacial area ratio; S_q = Root mean square height; S_{sk} = Skewness; S_{ku} = Kurtosis.

___

3.4   Electrical characterization

Resistance measurements

As previously discussed, the growth of PEDOT fibers is inherently random. For this reason, resistance analysis was conducted using a statistical approach. Measurements were taken on PEDOT and PEDOT/P3HT samples, both before and after the P3HT coating.

P3HT-only fibers are not included in this section, as their resistance values were comparable to an open circuit and therefore not relevant for the scope of this study. Nonetheless, considering the presence in literature of studies that demonstrate high conductivity achieved with P3HT through different strategies[77,78,79], much more can be investigated in this direction.
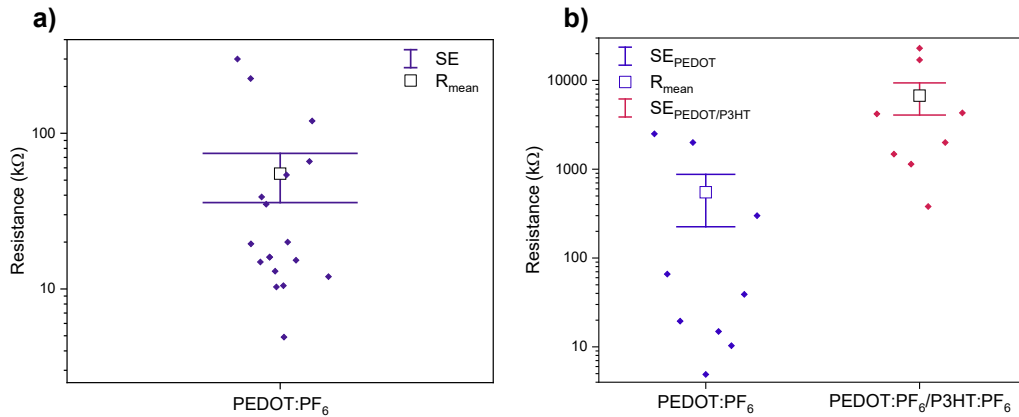
Figure 3.13: Distribution of the resistances over the all PEDOT:PF$_6$ samples below MΩ (a) and of a selection of samples before (blue) and after P3HT coating (red), with related mean value (square) and standard error.

___

The resistance measurements for PEDOT samples in Fig. 3.13a show the distribution of resistances measured on the PEDOT fibers that has reached saturation during the polymerization. Indeed, as explained in Sec. 1.4, fibers grow until the resistance drops sufficiently down to hamper polymerization. This should result in resistance values

within a consistent range, with variation attributed to fiber morphology. Fibers exhibiting excessively high resistance are likely those that did not reach saturation and can be safely excluded from this analysis.

The average resistance across the full PEDOT dataset was found to be 55 kΩ,a moderately low value, though not sufficient to ensure enough conduction. Nonetheless, most of the samples are concentrated between 10 kΩ and 20 kΩ, a range of values that can enable the testing of the device as a transistor. Despite the presence of better-performing devices, the high variance leads to a low yield of functional samples.

Two additional factors must be considered when interpreting resistance measurements. The first is the doping level of the polymer. Immediately after polymerization, fibers exhibit high doping, resulting in lower resistance values. While some fibers remain stable, others show significant reduction of the doping level over time, that can be roughly estimated by their change in color. The second factor is material degradation, which is particularly difficult to assess in large and topologically diverse samples using resistance alone.

The results of investigation to assess whether the application of a P3HT coating alters the resistance are represented in Fig. 3.13b. Measurements taken before and after coating showed an increase of nearly two orders of magnitude, with average resistance rising from 500 kΩ to 3.42 MΩ. In general, an increase of 1-2 orders of magnitude was consistently observed across nearly all analyzed samples.

Two hypotheses are proposed. Given the intrinsic porosity of PEDOT, it is possible that the 3HT monomer solution infiltrates the polymer matrix, initiating polymerization internally. This would result in the formation of a heterojunction, potentially impacting the measured resistance. Alternatively, it is possible that during cyclic voltammetry used for P3HT polymerization, PEDOT may undergo reduction, losing dopant content, becoming less conductive, representing a drawback for optimal OECT operation. However, further investigations could be undertaken to enhance this property.

OECT operation

To operate as OECTs, the samples must exhibit low resistance, on the order of a few kΩ, since the ON-state current is highly dependent on the fiber characteristics when the gate potential is zero. In our case, the lowest measured resistances were in the 10–20 kΩ range, and even small variations in resistance and fiber topology led to drastically different outcomes.

The sample selected for OECT testing is the one already shown in Fig. 3.2, that was characterized by high diffusive fibers. The measured resistance is 13.3 kΩ.

As discussed in Section 1.5.1, due to potential drops at the electrolyte interfaces, the effective zero of the gate voltage is shifted toward negative values, for this reason both polarities of gate voltages must be investigated. Figure 3.14 shows the output characteristics measured with gate voltages ranging from -400 mV to $+600$ mV, and drain voltages from 0 to -800 mV. For low V_{DS} values, the device behaves linearly, as conduc-

tion occurs through the entire bulk of the fiber in a resistive manner. For higher drain voltages, saturation is not clearly visible in all curves. In fact, for negative gate voltages, saturation likely occurs at higher drain values. When the gate voltage increases, channel conduction is already sufficiently limited to induce saturation within the tested range.
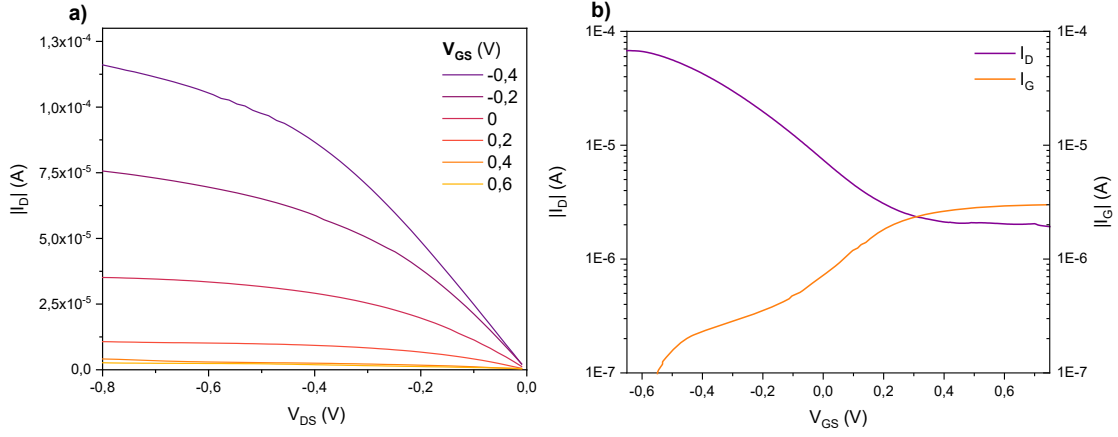
Figure 3.14: Results of measurement of the sample in Fig. 3.2d. operating as OECT. (a) output characteristics at different gate voltages from -0.4 to 0.6 and (b) transfer characteristics with drain current (purple) and gate current (organge).

Gate voltage modulation of the channel current can also be observed. For $V_{GS} < 0\,\text{V}$, current levels differ significantly between curves, whereas for positive gate voltages, relative variations become much smaller. A threshold voltage around $V_{GS} = 400\,\text{mV}$ can be assumed, beyond which no appreciable changes are observed.

The transfer characteristic in Fig. 3.14b was obtained with $V_{DS} = -400\,\text{mV}$, using a gate voltage sweep from $-650\,\text{mV}$ to $+800\,\text{mV}$. Although this drain voltage is near the limit of the transistor's linear region, it was chosen to allow for the observation of more significant currents. At $V_{DS} = -0.6\,\text{V}$, the device is in the ON state, and the current reaches a maximum of $I_{ON} = 66.7\,\mu\text{A}$, corresponding to the fiber's resistive response. Below this voltage, the current does not vary significantly.

As the gate voltage increases, ions are driven into the channel and the device begins to turn off, reaching a plateau at approximately $V_{GS} = 0.5\,\text{V}$, with a corresponding OFF-state current of $I_{OFF} = 2.1\,\mu\text{A}$. These values result in an I_{ON}/I_{OFF} ratio of 30. While not exceptional for this type of device, they must be considered in light of the fiber's geometrical characteristics. The calculated threshold voltage (V_{th}) is 0.23 V.

As already mentioned, the fiber forming the channel is still too long, and thus has high resistance. Furthermore, the polymerization conditions strongly affect the resulting fiber, producing topologies different from previously studied devices. As highlighted by Janzakova[47], thinner and smaller fibers tend to be easier to switch off, as ions can penetrate and dedope the polymer more easily. In contrast, the fiber shown in Figure 3.2 is relatively thick, so limited switching performance is expected. Fibers grown under conditions where diffusion plays a more prominent role, as in this case, as confirmed by the fractal analysis in Sec. 3.3, are clearly disadvantaged in terms of switching behavior.

This reveals a trade-off between reducing resistance by increasing fiber width and achieving better switching with thinner fibers, which allow for lower plateau currents. Even if a higher doping level were obtained, with this fiber geometry it would not translate into significantly improved switching performance.

Another key parameter for OECTs is transconductance. PEDOT-based devices are widely recognized for their high g_m values compared to other electrolyte-operated transistors, with reported values often in the mS range or higher[36]. In our device, the maximum transconductance measured was $g_m = 138 \, \mu S$, an order of magnitude less than other high performance devices, which considering the limitations of the device geometry, not optimized for high performance, represents a fair result.

Moreover, it is important to specify that the target of this work is not to obtain a high performance device, but rather to demonstrate that even with such non-idealities the conductivity of the fiber can be modulated

It is also important to note that the transconductance peak occurs at $V_{GS} = -0.45 \, V$, a value close to the ON-state. This detail may be relevant for applications such as reservoir computing, where large responses to small stimuli are required. A transconductance peak shifted away from equilibrium ($V_{GS} = 0$) is a limiting factor, reducing the system's sensitivity to complex signals. This is particularly relevant in scenarios such as those described by Cucchi et al.[8], where distorted sinusoidal signals centered around zero are used. However, the study from Weissbach *et al.*[80] showed that it is possible to shift the position of the transfer characteristics in a more extended electronic circuit. In this way, the position of the transconductance can be tuned as needed.

The cause of this shift remains unclear and may be attributed either to measurements performed near the edge of the transistor's linear region, or to intrinsic properties of the fiber itself, which—as previously discussed—does not have an optimal structure for effective dedoping under gate bias.

In conclusion, this study demonstrated that fiber-based channels can still achieve current modulation, even under non-ideal conditions. To improve performance, future efforts should focus on producing thinner and less resistive fibers. The strong dependence of device behavior on fiber resistivity, as confirmed in this study, is of interest for neuromorphic applications, since the fiber resistance can be finely tuned during polymerization. This enables the modulation of conductance in a way that mimics synaptic weighting in biological systems.

3.5   Optical measurements on PEDOT/P3HT fibers

UV-VIS absorption

The absorption measurement of the sample prepared as described in Sec. 2.3.3 resulted in the absorption profile shown in Fig. 3.15. Compared to the spectrum of pure P3HT, a blue-shift of the main absorption peak is observed, from 535 nm to 480 nm. Considering that also the electrodeposited P3HT absorption peak shows a shift with respect to literature to 490 nm, the chance in absorption spectrum can to be attributed to the deposition technique. Indeed, this shift may originate from the different organization of the polymer film during polymerization and on the PEDOT surface, considering its high porosity and the hypothesis that P3HT polymerization occurs also within the polymeric matrix. Several studies have demonstrated that the morphology of P3HT affects the bandgap energy, and thus its absorption properties[81,74,82]. Moreover, similar shifts has been shown in the study of Rahimi *et al.*[83] with the reduction of cristallinity of P3HT up to the maximum shift obtained with P3HT liquid solution. In the present case, a reduced regioregularity is expected, which would result in a wider bandgap and, consequently, a shift towards shorter wavelengths. Further investigations are required to explore the influence of P3HT regioregularity on the absorption features, potentially including the role of thermal annealing, which has been reported to significantly affect polymer reorganization.
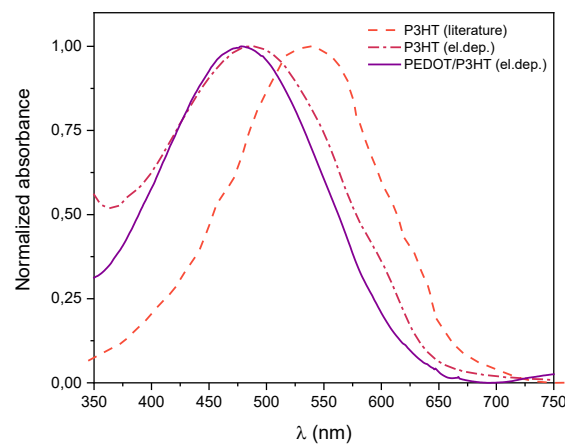
Figure 3.15: Plot of the adsorbance measured with UV-Vis spectrophotometer of PEDOT/P3HT film (solid line) and P3HT film (dash-dot-line) compared to the reference of pure P3HT from literature[84] (dash-line).

_____

Photo-active response

Despite the limitations discussed earlier, nearly all fibers coated with P3HT displayed a measurable photovoltage response. However, the intrinsic differences between samples resulted in a large variance when averaging the measurements, which also tended to obscure the individual features of the device response. In particular, the shape of the curves and peaks varied significantly across devices, often displaying unstable or unpredictable

responses. In some cases, the measured voltage started fluctuating irregularly after some expositions, showing values that were either unexpected or random.

Such complex phenomenons can be attributed to multiple causes. First, considering that the behavior of OMIECs and OECTs is not yet fully understood, the system implemented here adds a further layer of complexity. The presence of a photoelectrochemical cell, which involves interactions with the electrolyte, already constitutes a significant challenge. Additionally, the fibers were not produced using an ideal setup, diffusive phenomena played a dominant role during polymerization, deviating from what is commonly reported in the literature. The electropolymerized P3HT coating of PEDOT fibers has also not been previously studied, and thus new types of interactions could emerge, requiring further and separate investigation. For instance, a strudy from Tahmani et $al.$[85] reported switching behavior in PEDOT/P3HT heterojunctions. Although the structure here is different, similar interactions may occur and could help explain some of the anomalous results, together with a better understanding of the ionic counterpart.

This section reports the optical response of a representative device, already showed in Fig. 3.10b, which demonstrated stable behavior across repeated measurements and a peak shape consistent with the other less stable measurements. This allowed for the extraction of quantitative features of the photoresponse. Figure 3.16 shows the overlay open-circuit voltage (V_{OC} peaks measured in the horizontal configuration and in the vertical configuration as explained in Sec. 2.3.3. The various peaks correspond to different light intensities in percentage with respect to the maximum amplitude possible.
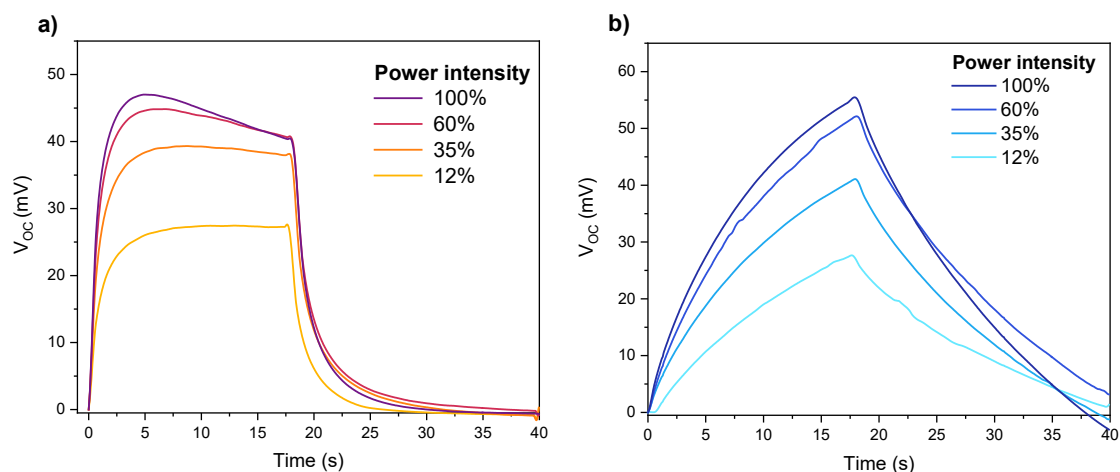
Figure 3.16: Overlay of the peaks with growing power intensities measured between the gold contacts (horizontal)(a) and from short-circuited contacts to a Pt electrode in solution (vertical)(b).

It can be observed that the shape of the peaks resembles the one of a RC circuit, even if with different time constants. This can be explained considering the mechanism already discussed in Sec. 1.5.4, where charges gradually accumulate between the electrolyte and the conductive polymers, with time constants governed by the resistance and volumetric capacitance of the fiber. On the other hand it is not as easy to explain the differences

in shapes and peak height observed between horizontal and vertical measurements.

Fig. 3.17a shows how the open-circuit voltage (V_{OC}) varies with LED power in both the horizontal and vertical configurations. Fig. 3.17b reports the same measurement as a function of LED wavelength at constant power. In the first case, V_{OC} increases with power, and the vertical configuration consistently shows higher values, especially at higher powers. In the second case, V_{OC} in general increases as wavelength decreases, with also the difference between the two configurations becoming less pronounced. At shorter wavelengths, the horizontal measurement equals and surpasses the vertical one.
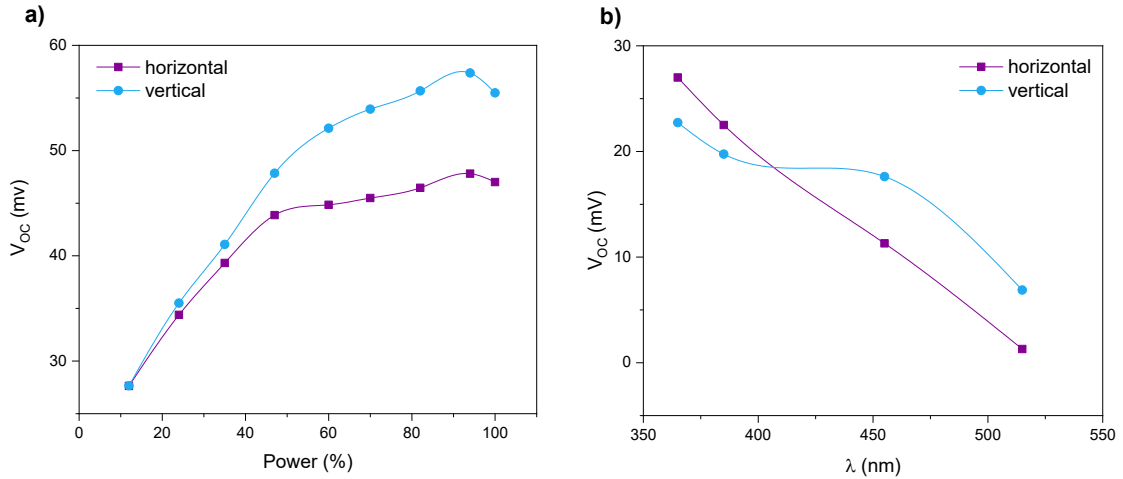
Figure 3.17: Maximum peak value measured on the V_{OC} for both horizontal and vertical configuration, depending on power intensity (a) and on the wavelength (b).

These results differ from what is expected considering the absorption spectrum measured with the spectrophotometer, where the absorption peak was at 480 nm. A few considerations can be made in this regard. First, the $PEDOT:PF_6/P3HT:PF_6$ spectrum does not drop too sharply after the peak, but the absorption is still non negligible even for the LED wavelengths used (455 nm, 385 nm, and 365 nm). Then it is also important to note that LED emissions are not truly monochromatic but span a broader spectrum. Furthermore, as discussed in Sec. 2.3.3, there is no accurate calibration of the LED irradiance on the sample, so the actual light power may differ between colors. These aspects require further analysis before reaching definite conclusions.

For the same reasons, it is difficult to compare the V_{OC} values obtained under white light with those from individual monochromatic LEDs, as white LEDs typically emit across a broader spectrum and may have higher total power.

Peak response times were analyzed through nonlinear fitting of the decay portion of the photovoltage signal after LED switch-off. The results showed a good fit with a single exponential decay, while the rise part of the curve during LED illumination did not produce reliable fits. Fig. 3.18 display the extracted discharge time constants, $\tau_{discharge}$. No significant correlation between white light power and $\tau_{discharge}$ was observed. However, a clear difference is found between horizontal and vertical configurations Fig.(3.18a). In

the horizontal case, both charging and discharging are faster, as also seen in Fig. 3.16, where the V$_{OC}$ saturates quickly, unlike in the vertical case. The dependence of $\tau_{\text{discharge}}$ on wavelength also differs between the two configurations, though the difference decreases at shorter wavelengths (Fig. 3.18b). Values also differ from those measured under white light, again likely due to different power levels and spectral distributions.
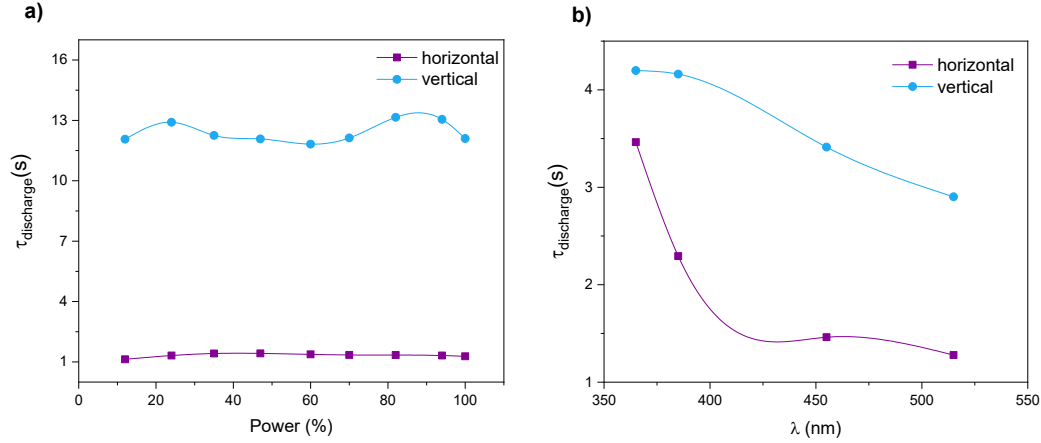
Figure 3.18: Half-life (τ) obtained with exponential fitting of the discharge curve for both horizontal and vertical configuration, depending on power intensity (a) and on the wavelength (b).

The reasons behind the difference between horizontal and vertical configurations require further investigation. They may lie in the particular characteristics of the examined device, or in how the photovoltage is measured. While a photovoltage in the vertical setup was expected based on the theory discussed in Sec. 1.5.4, the horizontal response is novel, especially since its magnitude is similar.

Although further validation is needed, a plausible explanation is that the same mechanism occurs in both configurations. Upon illumination, excitons are separated in the P3HT π-stacking regions. Due to asymmetries in carrier mobility, holes diffuse more rapidly, reaching the PEDOT interface, where mobility and charge density are higher. Electrons, on the other hand, already suffer from low mobility and are further trapped by dissolved oxygen, forming superoxide and reducing electron transport. The system thus accumulates charge like a capacitor: positive in the gold electrodes and negative in the electrolyte. Since the platinum wire in the electrolyte was connected to the positive terminal of the measurement system, the observed voltage was consistently negative, supporting this hypothesis. The role of the electrolyte also deserves investigation, as ion drift could contribute to the behavior.

Unlike in the vertical configuration, the horizontal one sometimes produced positive peaks and sometimes negative ones, depending on the sample. Moreover, horizontal photovoltage response is harder to explain. Theoretically, the two electrodes should be symmetrical with respect to the fiber and accumulate equal charge, producing no net voltage. However, asymmetries in fiber morphology could lead to large differences in resistance along the path between electrodes. Charge separation occurs along the entire

fiber, and charges may diffuse toward one electrode more than the other, depending on the local resistance and carrier mobility. What is likely measured, then, is the voltage difference between two unequally charged electrodes.

This hypothesis could be confirmed by comparing the voltage of each individual electrode with the vertical measurement. In our case such measurements were unstable and inconclusive, highlighting that better control over fiber growth and morphology is needed, to allow clearer insights into these asymmetric effects and separate photovoltage contributions.

In conclusion, a more accurate study of the influence of characteristics of the fibers, i.e. morphology, resistance, capacity and doping, could lead to more detailed explanations about the effective reasons behind this behavior

3.6   Cells viability

To date, the biocompatibility of polymeric fibers produced via AC-electropolymerization has never been demonstrated, although this property represents a critical step towards ensuring the actual implantability of these devices in biological environments. Considering the specific fabrication approach adopted, it is essential to evaluate if and how this procedure might influence the compatibility of the fibers with living tissue. Future studies should investigate whether cells prefer highly porous substrates over conventional ones. However, the significant porosity of these polymers might cause retention of cytotoxic substances such as monomers and salts within the polymer matrix, potentially affecting cell viability.

As an initial step towards verifying the suitability of these fibers for further biological studies, a preliminary morphological analysis of cells cultured on the fibers was conducted. The shape and structure of cells (morphology) can influence their functions as a predictive screening; by analyzing cell morphology, it is possible to quickly screen and identify the most promising materials for further development, saving time and resources in the bio-material design process. Evaluating the cell's morphology can indicate how well a material is tolerated by the *in-vitro* system and potentially in the human body. Abnormal cell shapes might suggest cytotoxicity or poor compatibility, which is critical for ensuring the safety and effectiveness of the medical applicability of the material of interest. For these reasons, the evaluation of the morphology of the SH-SY5Y cells was performed by considering a sample of control (CTRL) and samples with the fibers made with PEDOT:P3HT. SH-SY5Y cells were seeded and cultured on the fibers for 24 hours. Bright-field acquisitions of cells in contact with the fibers were made to examine the cell's morphology. As visible from Fig. 3.19, the cells proliferate and interact perfectly with the samples of interest. They maintain a similar morphology across all samples, indicating proper behavior both in contact with the control sample and the fiber-containing samples. Even more, multilayer cellular networks and multidirectional cell-cell interactions were established.
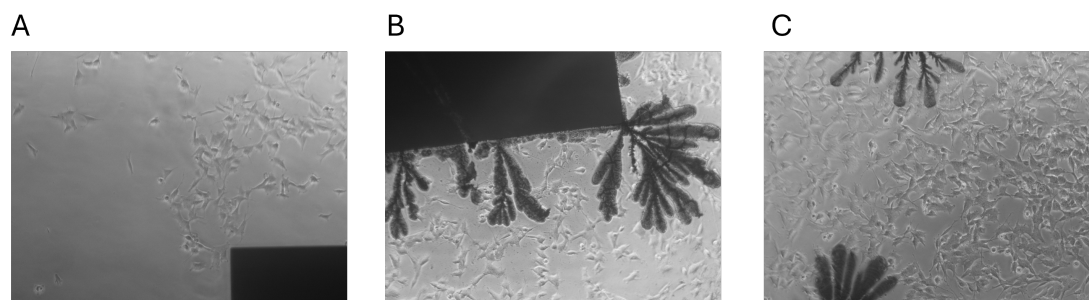
Figure 3.19: Bright field images of shy cells (A) on the control sample, (B) and (C) on the fibers made with PEDOT and P3HT coating.

CHAPTER 4

Conclusion and outlook

At the conclusion of this work, it is necessary to critically review the achieved results, highlighting both the strengths and limitations in order to define the most promising directions for future developments. The initial goals set out in the motivation were: (i) to obtain conductive PEDOT fibers responsive to applied potentials in solution, (ii) to fabricate fibers exhibiting photoactivity, and (iii) to demonstrate the viability of cells on the polymer-coated substrates.

OBeyond this verification, it is essential to revisit some of the fundamental steps that led to the achieved results. The work was carried out without a predefined experimental framework in the laboratory: both the device and the electropolymerization protocol were customized from scratch. The initial absence of a dedicated mask and the need to adapt the architecture from a different lithographic layout required the testing of multiple mask geometries and substrates before converging on the final solution. Although the selected design proved to be the most effective among various attempts, it still presents limitations, extensively discussed in the methods section.

One of the first and most unexpected issues was the corrosion of the electrical contacts. Despite several hypotheses, the underlying mechanism remains unclear and should be investigated further. The only viable approach was to identify a narrow operating window that allowed polymer growth without damaging the electrodes. This constraint was highly sensitive to the solution chemistry. Numerous dopant-solvent combinations were tested before selecting the one adopted in this work. Although other formulations did not produce stable growth, further optimization under improved conditions may enable their future use.

Another major challenge was the long growth time of fibers before bridging, which necessitated the design of a sealed and stable reaction chamber. A custom plastic well was developed after several trials, and attached to the substrate with special attention to reliable bonding using biocompatible adhesives. Leakage issues in the early stages significantly affected reproducibility, but were later mitigated by optimizing the sealing method. Constructing an electropolymerization setup compatible with the confined chamber geometry also required substantial technical effort.

The successful electropolymerization of P3HT into fiber structures, never previously reported in literature, represents one of the key outcomes of this work. However, their high resistance and low mechanical stability prevented consistent electrical characterization. Although some optical responses were observed, limited reproducibility and the frequent appearance of random artifacts in measures excluded them from the conclusive results. Future investigations based on an optimized device layout could better clarify the potential of this configuration.

A significant step forward was achieved through the fabrication of hybrid PEDOT/P3HT fibers, where PEDOT acted as a hole-transporting layer. This bilayer structure enabled more stable photoresponses, though open-circuit voltage signals displayed large variability in both amplitude and discharge dynamics. These limitations prevented statistical analysis across devices; nonetheless, a tighter control of growth parameters could improve reproducibility and enable a more in-depth exploration of the underlying mechanisms.

Nonetheless, to support these developments a new lithographic mask was designed and fabricated, marking a substantial improvement over previous prototypes. This includes two designs: one with a two-electrode configuration featuring 200 µm and 300 µm gaps, and another with a reservoir geometry comprising eight electrodes arranged around a circle with diameter 400 µm. Both designs incorporate a dedicated passivation mask, to be fabricated using SU-8 photoresist, aimed at minimizing leakages and enhancing again the reproducibility. A screen-printed Ag/AgCl gate electrode can also be integrated to enable a reliable OECT operation even without the electrode in solution from the top.
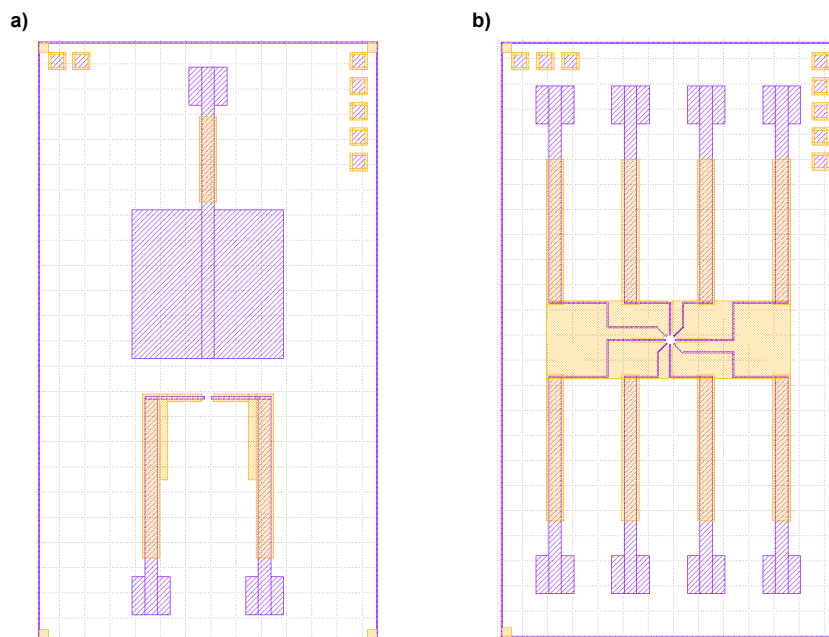
Figure 4.1: Improved mask design for fiber growth (purple). Device (a) is thought to standardize the studied about AC-electropolymerization of PEDOT and P3HT. Device (b) features a 8 electrode configuration for preliminary test of neuromorphic fratures aiming for reservoir computing. In all che design a passivation layer has been included (orange).

Experimental results confirmed that PEDOT:PF$_6$ fibers, grown with an optimized AC-electropolymerization protocol, maintain electrochemical switching behavior even at larger scales. This observation supports their suitability for integration into neuromorphic systems involving biological interfaces. Additionally, fibers coated with P3HT showed measurable photovoltage generation, influenced by the electrolyte composition, suggesting the presence of a shared potential needed for nonlinear interactions. Short-term memory effects observed in PEDOT/P3HT bilayer structures under illuminations further emphasize their relevance for neuromorphic computing. Nonetheless, the resistance of such fibers is still too low and most of the observed behaviors cannot be explained yet and require further investigation.

In summary, this work achieved the following advancements:

- developed a PEDOT:PF$_6$ fiber growth protocol tailored to a custom microelectrode architecture;

- observed long-timescale AC-electropolymerization dynamics distinguishing between field-driven and diffusion-limited regimes;

- fabricated PEDOT fibers functional as OECTs under suboptimal geometries;

- demonstrated, for the first time, the electropolymerization of P3HT into fiber-like structures;

- produced hybrid PEDOT/P3HT bilayer fibers with photoresponses;

- performed preliminary biocompatibility testing validating the system for bioelectronic use.

Although some aspects of this research still require refinement, the framework developed here provides a solid and original basis for future studies. The methodologies, design strategies, and experimental observations reported in this thesis are expected to contribute to the development of advanced neuromorphic systems at the Sensing Technologies group. Future directions should focus on improving long-term device stability, increasing growth reproducibility, and advancing the biological integration of polymer-based OECTs, paving the way toward complex biohybrid computing architectures capable of performing sophisticated signal processing in liquid-phase environments.

List of Figures

Bibliography

[1] Anmona Shabnam Pranti, Andreas Schander, André Bödecker, and Walter Lang. Pedot: Pss coating on gold microelectrodes with excellent stability and high charge injection capacity for chronic neural interfaces. *Sensors and Actuators B-chemical*, 2018.

[2] Peter D Jones, Anastasiya Moskalyuk, Clemens Barthold, Katja Gutöhrlein, Gerhard Heusel, Birgit Schröppel, Ramona Samba, and Michele Giugliano. Low-impedance 3d pedot: Pss ultramicroelectrodes. *Frontiers in Neuroscience*, 14:405, 2020.

[3] Diego Ghezzi, Maria Rosa Antognazza, Rita Maccarone, Sebastiano Bellani, Erica Lanzarini, Nicola Martino, Maurizio Mete, Grazia Pertile, Silvia Bisti, Guglielmo Lanzani, and Fabio Benfenati. A polymer optoelectronic interface restores light sensitivity in blind rat retinas. *Nature Photonics*, 2013.

[4] Susana Vaquero, Caterina Bossio, Sebastiano Bellani, Nicola Martino, Elena Zucchetti, Guglielmo Lanzani, and Maria Rosa Antognazza. Conjugated polymers for the optical control of the electrical activity of living cells. *Journal of Materials Chemistry B*, 2016.

[5] Paschalis Gkoupidenis, Nathan Schaefer, Xenofon Strakosas, Jessamyn A. Fairfield, and George G. Malliaras. Synaptic plasticity functions in an organic electrochemical transistor. *Applied Physics Letters*, 2015.

[6] Matteo Cucchi, Hans Kleemann, Hsin Tseng, Giuseppe Ciccone, Alexander Lee, Darius Pohl, and Karl Leo. Directed growth of dendritic polymer networks for organic electrochemical transistors and artificial synapses. *Advanced Electronic Materials*, 7(10):2100586, 2021.

[7] Kamila Janzakova, Ismael Balafrej, Ankush Kumar, Nikhil Garg, Corentin Scholaert, Jean Rouat, Dominique Drouin, Yannick Coffinier, Sébastien Pecqueur, and Fabien Alibart. Structural plasticity for neuromorphic networks with electropolymerized dendritic pedot connections. *Nature Communications*, 14(1):8143, 2023.

[8] Matteo Cucchi, Christopher Gruener, Lautaro Petrauskas, Peter Steiner, Hsin Tseng, Axel Fischer, Bogdan Penkovsky, Christian Matthus, Peter Birkholz, Hans Kleemann, et al. Reservoir computing with biocompatible organic electrochemical networks for brain-inspired biosignal classification. *Science Advances*, 7(34):eabh0693, 2021.

[9] Jonathan Rivnay, Roisin M. Owens, Róisín M. Owens, and George G. Malliaras. The rise of organic bioelectronics. *Chemistry of Materials*, 2014.

[10] Olga Bubnova, Zia Ullah Khan, Hui Wang, Slawomir Braun, Drew R Evans, Manrico Fabretto, Pejman Hojati-Talemi, Daniel Dagnelund, Jean-Baptiste Arlin, Yves H Geerts, et al. Semi-metallic polymers. *Nature materials*, 13(2):190–194, 2014.

[11] Beatrice Fraboni Filippo Bonafè, Francesco Decataldo and Tobias Cramer. Charge carrier mobility in organic mixed ionic–electronic conductors by the electrolyte-gated van der pauw method. *Advanced electronic materials*, 2021.

[12] Eleni Stavrinidou, Pierre Leleux, Harizo Rajaona, Dion Khodagholy, Jonathan Rivnay, Manfred Lindau, Sébastien Sanaur, and George G. Malliaras. Direct measurement of ion mobility in a conducting polymer. *Advanced Materials*, 2013.

[13] Nir Tessler, Yevgeni Preezant, Noam Rappaport, and Yohai Roichman. Charge transport in disordered organic materials and its relevance to thin-film devices: a tutorial review. *Advanced Materials*, 21(27):2741–2761, 2009.

[14] Magatte N Gueye, Alexandre Carella, Jérôme Faure-Vincent, Renaud Demadrille, and Jean-Pierre Simonato. Progress in understanding structure and transport properties of pedot-based materials: A critical review. *Progress in Materials Science*, 108:100616, 2020.

[15] Rodrigo Noriega, Jonathan Rivnay, Koen Vandewal, Felix PV Koch, Natalie Stingelin, Paul Smith, Michael F Toney, and Alberto Salleo. A general relationship between disorder, aggregation and charge transport in conjugated polymers. *Nature materials*, 12(11):1038–1044, 2013.

[16] Anton V Volkov, Kosala Wijeratne, Evangelia Mitraka, Ujwala Ail, Dan Zhao, Klas Tybrandt, Jens Wenzel Andreasen, Magnus Berggren, Xavier Crispin, and Igor V Zozoulenko. Understanding the capacitance of pedot: Pss. *Advanced Functional Materials*, 27(28):1700329, 2017.

[17] Jonathan Rivnay, Sahika Inal, Alberto Salleo, Roisin M Owens, Magnus Berggren, and George G Malliaras. Organic electrochemical transistors. *Nature Reviews Materials*, 3(2):1–14, 2018.

[18] Seiya Watanabe, Hiroaki Shibakita, Naruki Hagiwara, Ryosuke Nakajima, Hiroyuki S. Kato, and Megumi Akai-Kasaya. Pedot:pss wire: A two-terminal synaptic device for operation in electrolyte and saline solutions. *ACS Applied Materials and Interfaces*, 2024.

[19] Yuki Koizumi, Naoki Shida, Masato Ohira, Hiroki Nishiyama, Ikuyoshi Tomita, and Shinsuke Inagi. Electropolymerization on wireless electrodes towards conducting polymer microfibre networks. *Nature Communications*, 7(1):10404, 2016.

[20] Naruki Hagiwara, Shoma Sekizaki, Yuji Kuwahara, Tetsuya Asai, and Megumi Akai-Kasaya. Long-and short-term conductance control of artificial polymer wire synapses. *polymers*, 13(2):312, 2021.

[21] Naruki Hagiwara, Tetsuya Asai, Kota Ando, and Megumi Akai-Kasaya. Fabrication and training of 3d conductive polymer networks for neuromorphic wetware. *Advanced Functional Materials*, 33(42):2300903, 2023.

[22] Max Eickenscheidt, Eva Singler, and Thomas Stieglitz. Pulsed electropolymerization of pedot enabling controlled branching. *Polymer Journal*, 2019.

[23] Masafumi Ohira, Masato Ohira, Yuki Koizumi, Hiroki Nishiyama, Ikuyoshi Tomita, and Shinsuke Inagi. Synthesis of linear pedot fibers by ac-bipolar electropolymerization in a micro-space. *Polymer Journal*, 2017.

[24] Megumi Akai-Kasaya, Megumi Akai, Megumi Akai-Kasaya, Naruki Hagiwara, Wataru Hikita, Masaru Okada, Yasumasa Sugito, Yuji Kuwahara, and Tetsuya Asai. Evolving conductive polymer neural networks on wetware. *Japanese Journal of Applied Physics*, 2020.

[25] Giuseppe Ciccone, Matteo Cucchi, Yanfei Gao, Ankush Kumar, Lennart Maximilian Seifert, Anton Weissbach, Hsin Tseng, Hans Kleemann, Fabien Alibart, and Karl Leo. Growth and design strategies of organic dendritic networks. *Discover Materials*, 2(1):7, 2022.

[26] Côme Bodart, Nicolò Rossetti, Jo'Elen Hagler, Pauline Chevreau, Danny Chhin, Francesca Soavi, Steen B. Schougaard, Florin Amzica, and Fabio Cicoira. Electropolymerized poly(3,4-ethylenedioxythiophene) (pedot) coatings for implantable deep-brain-stimulating microelectrodes. *ACS Applied Materials & Interfaces*, 2019.

[27] Christoph Nick, Christiane Thielemann, and Helmut F. Schlaak. Pedot:pss coated gold nanopillar microelectrodes for neural interfaces. *International Conference on Manipulation, Manufacturing and Measurement on Nanoscale*, 2014.

[28] Sofia M Fonseca, Tiago Moreira, A Jorge Parola, Carlos Pinheiro, and César AT Laia. Pedot electrodeposition on oriented mesoporous silica templates for electrochromic devices. *Solar Energy Materials and Solar Cells*, 159:94–101, 2017.

[29] Eider A Erazo, Pablo Ortiz, and María T Cortés. Tailoring the pedot: Pss hole transport layer by electrodeposition method to improve perovskite solar cells. *Electrochimica Acta*, 439:141573, 2023.

[30] Erin L. Ratcliff, Judith M. Jenkins, Judith L. Jenkins, Kenneth W. Nebesny, Ken W. Nebesny, Neal R. Armstrong, and Neal R Armstrong. Electrodeposited, "textured" poly(3-hexyl-thiophene) (e-p3ht) films for photovoltaic applications. *Chemistry of Materials*, 2008.

[31] SC Perry, Sasikumar Arumugam, Stephen Beeby, and I Nandhakumar. Template-free nanostructured poly-3-hexylthiophene (p3ht) films via single pulse-nucleated electrodeposition. *Journal of Electroanalytical Chemistry*, 933:117278, 2023.

[32] Matteo Cucchi. *Organic electrochemical networks for biocompatible and implantable machine learning*. PhD thesis, Faculty of Physics, TU Dresden, 2022.

[33] Hsin Tseng, Matteo Cucchi, Anton Weissbach, Karl Leo, and Hans Kleemann. Membrane-free, selective ion sensing by combining organic electrochemical transistors and impedance analysis of ionic diffusion. *ACS Applied Electronic Materials*, 3(9):3898–3903, 2021.

[34] Daniel A. Bernards and George G. Malliaras. Steady-state and transient behavior of organic electrochemical transistors. *Advanced Functional Materials*, 2007.

[35] Jonathan Rivnay, Pierre Leleux, Marc Ferro, Michele Sessolo, Adam Williamson, Dimitrios A. Koutsouras, Dion Khodagholy, Marc Ramuz, Xenofon Strakosas, Roisin M. Owens, Róisín M. Owens, Christian Bénar, Christian G. Bénar, Jean-Michel Badier, Jean-Michel Badier, Christophe Bernard, George G. Malliaras, and Georgios Malliaras. High-performance transistors for bioelectronics through tuning of channel thickness. *Science Advances*, 2015.

[36] Dion Khodagholy, Jonathan Rivnay, Michele Sessolo, Moshe Gurfinkel, Pierre Leleux, Leslie H Jimison, Eleni Stavrinidou, Thierry Herve, Sébastien Sanaur, Róisín M Owens, et al. High transconductance organic electrochemical transistors. *Nature communications*, 4(1):2133, 2013.

[37] Jacob T. Friedlein, Robert R. McLeod, and Jonathan Rivnay. Device physics of organic electrochemical transistors. *Organic Electronics*, 2018.

[38] Jacob T. Friedlein, Jonathan Rivnay, David Dunlap, David H. Dunlap, Iain McCulloch, Sean E. Shaheen, Robert R. McLeod, and George G. Malliaras. Influence of disorder on transfer characteristics of organic electrochemical transistors. *Applied Physics Letters*, 2017.

[39] Matteo Cucchi, Anton Weissbach, Lukas M. Bongartz, Richard Kantelberg, Hsin Tseng, Hans Kleemann, and Karl Leo. Thermodynamics of organic electrochemical transistors. *Nature Communications*, 2022.

[40] Paschalis Gkoupidenis, Dimitrios A. Koutsouras, and George G. Malliaras. Neuromorphic device architectures with global connectivity through electrolyte gating. *Nature Communications*, 2017.

[41] Paschalis Gkoupidenis, Nathan Schaefer, Benjamin Garlan, and George G Malliaras. Neuromorphic functions in pedot: Pss organic electrochemical transistors. *Advanced Materials*, 27(44):7176–7180, 2015.

[42] Sébastien Pecqueur, Maurizio Mastropasqua Talamo, David Guérin, David Guerin, Philippe Blanchard, Jean Roncali, D. Vuillaume, Dominique Vuillaume, and Fabien Alibart. Neuromorphic time-dependent pattern classification with organic electrochemical transistor arrays. *Advanced electronic materials*, 2018.

[43] Yoeri van de Burgt, Ewout Lubberman, Elliot James Fuller, Elliot J. Fuller, Scott T. Keene, Gregório Couto Faria, Sapan Agarwal, Matthew Marinella, Matthew J. Marinella, A. Alec Talin, and Alberto Salleo. A non-volatile organic electrochemical device as a low-voltage artificial synapse for neuromorphic computing. *Nature Materials*, 2017.

[44] Yoeri van de Burgt, Armantas Melianas, Scott T. Keene, George G. Malliaras, and Alberto Salleo. Organic electronics for neuromorphic computing. *null*, 2018.

[45] Jennifer Y. Gerasimov, Roger Gabrielsson, Robert Forchheimer, Eleni Stavrinidou, Daniel T. Simon, Daniel Simon, Magnus Berggren, and Simone Fabiano. An evolvable organic electrochemical transistor for neuromorphic applications. *Advanced Science*, 2019.

[46] Imke Krauhausen, Charles-Théophile Coen, Simone Spolaor, Paschalis Gkoupidenis, and Yoeri van de Burgt. Brain-inspired organic electronics: Merging neuromorphic computing and bioelectronics using conductive polymers. *null*, 2023.

[47] Kamila Janzakova, Ankush Kumar, Mahdi Ghazal, Anna Susloparova, Yannick Coffinier, Fabien Alibart, and Sébastien Pecqueur. Analog programing of conducting-polymer dendritic interconnections and control of their morphology. *Nature Communications*, 2021.

[48] Lautaro Petrauskas, Matteo Cucchi, Christopher Grüner, Frank Ellinger, Karl Leo, Christian Matthus, and Hans Kleemann. Nonlinear behavior of dendritic polymer networks for reservoir computing. *Advanced Electronic Materials*, 8(3):2100330, 2022.

[49] Corentin Scholaert, Yannick Coffinier, Sébastien Pecqueur, and Fabien Alibart. Brain-inspired polymer dendrite networks for morphology-dependent computing hardware. *arXiv.org*, 2024.

[50] Małgorzata Skorupa, Daria Więcławska, Dominika Czerwińska-Główka, Magdalena Skonieczna, and Katarzyna Krukiewicz. Dopant-dependent electrical and biological functionality of pedot in bioelectronics. *Polymers*, 13(12):1948, 2021.

[51] Zaid Aqrawe, Johanna M. Montgomery, Jadranka Travaš-Sejdić, Jadranka Travas-Sejdic, and Darren Svirskis. Conducting polymers for neuronal microelectrode array recording and stimulation. *Sensors and Actuators B-chemical*, 2018.

[52] Zaid Aqrawe, Bryon E. Wright, Nitish Patel, Yukti Vyas, Jenny Malmström, Johanna M. Montgomery, David E. Williams, Jadranka Travaš-Sejdić, Jadranka Travas-Sejdic, and Darren Svirskis. The influence of macropores on pedot/pss microelectrode coatings for neuronal recording and stimulation. *Sensors and Actuators B-chemical*, 2019.

[53] Christoph Nick, Helmut F. Schlaak, and Christiane Thielemann. Pedot:pss coated gold nanopillar microelectrodes with ultralow impedance for neural interfaces. *International Journal of Nanomanufacturing*, 2017.

[54] Mengge Wu, Kuanming Yao, Ningge Huang, Hu Li, Jingkun Zhou, Rui Shi, Jiyu Li, Xingcan Huang, Jian Li, Huiling Jia, et al. Ultrathin, soft, bioresorbable organic electrochemical transistors for transient spatiotemporal mapping of brain activity. *Advanced Science*, 10(14):2300504, 2023.

[55] Diego Ghezzi, Maria Rosa Antognazza, Marco Dal Maschio, Erica Lanzarini, Fabio Benfenati, and Guglielmo Lanzani. A hybrid bioorganic interface for neuronal photoactivation. *Nature Communications*, 2011.

[56] Paola Campione, Claudia Latte Bovio, Giovanna Calabrese, Francesca Santoro, and Grazia Maria Lucia Messina. P3ht-based electroactive films for in vitro neuronal cell interfacing. *Advanced Materials Interfaces*, page 2400776, 2025.

[57] José Fernando Maya-Vetencourt, José Fernando Maya-Vetencourt, Diego Ghezzi, Maria Rosa Antognazza, Elisabetta Colombo, Maurizio Mete, Paul Feyen, Andrea Desii, Ambra Buschiazzo, Mattia Di Paolo, Stefano Di Marco, Flavia Ticconi, Laura Emionite, Dmytro Shmal, Cecilia Marini, Ilaria Donelli, Giuliano Freddi, Rita Maccarone, Silvia Bisti, Gianmario Sambuceti, Grazia Pertile, Guglielmo Lanzani, and Fabio Benfenati. A fully organic retinal prosthesis restores vision in a rat model of degenerative blindness. *Nature Materials*, 2017.

[58] Vini Gautam, David G. Rand, David Rand, David M. Rand, Yael Hanein, and K. S. Narayan. A polymer optoelectronic interface provides visual cues to a blind retina. *Advanced Materials*, 2014.

[59] Carl Poelking, Kostas Daoulas, Alessandro Troisi, and Denis Andrienko. Morphology and charge transport in p3ht: a theorist's perspective. *P3HT Revisited–From Molecular Scale to Solar Cell Devices*, pages 139–180, 2014.

[60] Carl Poelking and Denis Andrienko. Effect of polymorphism, regioregularity and paracrystallinity on charge transport in poly (3-hexylthiophene)[p3ht] nanofibers. *Macromolecules*, 46(22):8941–8956, 2013.

[61] Xiao Mei Jiang, Ronald Österbacka, Oleg Korovyanko, Chong P An, Baruch Horovitz, René AJ Janssen, and Z Valy Vardeny. Spectroscopic studies of photoexcitations in regioregular and regiorandom polythiophene films. *Advanced Functional Materials*, 12(9):587–597, 2002.

[62] Paul R. Berger, M. Kim, and Min Jae Kim. Polymer solar cells: P3ht:pcbm and beyond. *Journal of Renewable and Sustainable Energy*, 2018.

[63] Xiaobo Shen, Weiguo Hu, and Thomas P Russell. Measuring the degree of crystallinity in semicrystalline regioregular poly (3-hexylthiophene). *Macromolecules*, 49(12):4501–4509, 2016.

[64] A Medrano-Solís, ME Nicho, and F Hernández-Guzmán. Study of dual electrochromic devices based on polyaniline and poly (3-hexylthiophene) thin films. *Journal of Materials Science: Materials in Electronics*, 28:2471–2480, 2017.

[65] Kanghyun Choi and Allen J Bard. Doping of the semiconducting polymer poly(3-hexylthiophene) (p3ht) in organic photoelectrochemical cells. *Journal of the American Chemical Society*, 142(35):14878–14888, 2020.

[66] Sebastiano Bellani, Daniele Fazzi, P. Bruno, Ester Giussani, Eleonora Valeria Canesi, Guglielmo Lanzani, Lanzani Guglielmo, and Maria Rosa Antognazza. Reversible p3ht/oxygen charge transfer complex identification in thin films exposed to direct contact with water. *Journal of Physical Chemistry C*, 2014.

[67] Sebastiano Bellani, M. Porro, Matteo Porro, Claudia Caddeo, Maria Ilenia Saba, Paulo B. Miranda, Alessandro Mattoni, Guglielmo Lanzani, and Maria Rosa Antognazza. The study of polythiophene/water interfaces by sum-frequency generation spectroscopy and molecular dynamics simulations. *Journal of Materials Chemistry B*, 2015.

[68] Edoardo Mosconi, Paolo Salvatori, Maria Ilenia Saba, Alessandro Mattoni, Sebastiano Bellani, Francesco Bruni, Beatriz Santiago González, Beatriz Santiago Gonzalez, Maria Rosa Antognazza, Sergio Brovelli, Guglielmo Lanzani, Hong Li, Jean-Luc Brédas, Jean-Luc Brédas, and Filippo De Angelis. Surface polarization drives photoinduced charge separation at the p3ht/water interface. *ACS energy letters*, 2016.

[69] Antonio Guerrero, Marta Haro, Sebastiano Bellani, Maria Rosa Antognazza, L. Meda, Laura Meda, Sixto Giménez, Sixto Gimenez, and Juan Bisquert. Organic photoelectrochemical cells with quantitative photocarrier conversion. *Energy and Environmental Science*, 2014.

[70] Frank E. Osterloh, Michael A. Holmes, Lilian Chang, Adam J. Moulé, and Jing Zhao. Photochemical charge separation in poly(3-hexylthiophene) (p3ht) films observed with surface photovoltage spectroscopy. *Journal of Physical Chemistry C*, 2013.

[71] Greta Chiaravalli, Giovanni Manfredi, Riccardo Sacco, and Guglielmo Lanzani. Photoelectrochemistry and drift–diffusion simulations in a polythiophene film interfaced with an electrolyte. *ACS applied materials & interfaces*, 13(30):36595–36604, 2021.

[72] Jun Kawahara, Peter Andersson Ersman, Isak Engquist, and Magnus Berggren. Improving the color switch contrast in pedot: Pss-based electrochromic displays. *Organic Electronics*, 13(3):469–474, 2012.

[73] D. Levasseur, Delphin Levasseur, Issam Mjejri, Thomas Rolland, and Aline Rougier. Color tuning by oxide addition in pedot:pss-based electrochromic devices. *Polymers*, 2019.

[74] Ralf Mauer, Marcel Kastler, and Frédéric Laquai. The impact of polymer regioregularity on charge transport and efficiency of p3ht: Pcbm photovoltaic devices. *Advanced Functional Materials*, 20(13):2085–2092, 2010.

[75] Tanwistha Ghosh, Jayanthy S Panicker, and Vijayakumar C Nair. Self-assembled organic materials for photovoltaic application. *Polymers*, 9(3):112, 2017.

[76] Larry S Liebovitch and Tibor Toth. A fast algorithm to determine fractal dimensions by box counting. *physics Letters A*, 141(8-9):386–390, 1989.

[77] Wei Han, Ming He, Myunghwan Byun, Bo Li, and Zhiqun Lin. Large-scale hierarchically structured conjugated polymer assemblies with enhanced electrical conductivity. *Angewandte Chemie*, 125(9), 2013.

[78] Matthew J Panzer and C Daniel Frisbie. High carrier density and metallic conductivity in poly (3-hexylthiophene) achieved by electrostatic charge injection. *Advanced Functional Materials*, 16(8):1051–1056, 2006.

[79] David Neusser, Claudia Malacrida, Michal Kern, Yannic M Gross, Joris van Slageren, and Sabine Ludwigs. High conductivities of disordered p3ht films by an electrochemical doping strategy. *Chemistry of Materials*, 32(14):6003–6013, 2020.

[80] Anton Weissbach, Matteo Cucchi, Hsin Tseng, Karl Leo, and Hans Kleemann. Unraveling the electrochemical electrode coupling in integrated organic electrochemical transistors. *Advanced Functional Materials*, 2023.

[81] Frank C. Spano. Absorption in regio-regular poly(3-hexyl)thiophene thin films: Fermi resonances, interband coupling and disorder. *Chemical Physics*, 2006.

[82] Carl Poelking and Denis Andrienko. Effect of polymorphism, regioregularity and paracrystallinity on charge transport in poly(3-hexylthiophene) [p3ht] nanofibers. *Macromolecules*, 2013.

[83] Khosrow Rahimi, Ioan Botiz, John Onyango Agumba, John O. Agumba, Sajedeh Motamen, Natalie Stingelin, and Günter Reiter. Light absorption of poly(3-hexylthiophene) single crystals. *RSC Advances*, 2014.

[84] Erkin Zakhidov, Mukhib Imomov, Vakhob Quvondikov, Sherzod Nematov, Ilkhom Tajibaev, Aziz Saparbaev, Irfan Ismail, Bilal Shahid, and Renqiang Yang. Comparative study of absorption and photoluminescent properties of organic solar cells based on p3ht: Pcbm and p3ht: Itic blends. *Applied Physics A*, 125:1–7, 2019.

[85] Mehr Khalid Rahmani, Sobia Ali Khan, Muhammad Farooq Khan, and Moon Hee Kang. Fully solution-processed organic rram device with highly stable butterfly-shaped hysteresis. *Materials Science and Engineering: B*, 282:115784, 2022.

Aknowledgements

At the end of this work and of this journey, I owe my sincere gratitude to all the people who made it possible for me to reach this point.

This has been a meaningful experience—one that allowed me to grow not only in terms of technical skills but also on a personal level. I initially thought I could manage everything on my own, that I would somehow find a way to make it through. The truth is, without the people I had the chance to meet along the way, I would have never stepped out of my comfort zone, nor would I have grown into the person I am today.

A special thanks goes to the supervisors of this thesis:

- to Professor Carlo Ricciardi, for kindly agreeing to supervise a thesis with rather unconventional features for our field of study.

- to Professor Luisa Petti, for welcoming me into her research group and providing all the necessary resources to carry out my work in the best possible conditions, as well as for her thoughtful and careful revision of this thesis.

- to Dr. Giuseppe Ciccone, for the trust he placed in me from the very beginning and for giving me the freedom to experiment, make mistakes, and learn from them through shared reflection. The countless hours of discussion and analysis we had were the foundation of this work. I am especially grateful to him for going far beyond what was strictly required of his role, and for showing me what it means to aim higher, inspired by curiosity, innovation, and ideas.

A heartfelt thank you to Martina, to whom this entire work is dedicated. Thank you for never letting me feel alone, for believing in me even on the hardest days, and for bearing with my most difficult moments while I was searching for a place to feel at home.

I wish to thank my parents, who have always done their utmost to support my education and to provide me with everything I needed to grow, while giving me the freedom to make mistakes and learn from them.

I also thank my sister Ilaria, who has often taken on challenges ahead of me and offered advice when I needed it. She was also instrumental in solving some of the technical issues I encountered during this work.

I am grateful to my colleague Simone, who introduced me to the world of Bolzano and helped guide my decision, despite the flood of questions I sent his way. His support and our conversations about the research environment helped shape my next steps.

My thanks extend to my friends from home—especially Alberto, Matteo, and Filippo—who have remained close companions over the years, always checking in on me and offering support, even when I was not the easiest person to deal with.